creative commons

COMMONS DEED

저작자표시-비영리-변경금지 2.0 대한민국

이용자는 아래의 조건을 따르는 경우에 한하여 자유롭게

- 이 저작물을 복제, 배포, 전송, 전시, 공연 및 방송할 수 있습니다.

다음과 같은 조건을 따라야 합니다:

저작자표시. 귀하는 원저작자를 표시하여야 합니다.

비영리. 귀하는 이 저작물을 영리 목적으로 이용할 수 없습니다.

변경금지. 귀하는 이 저작물을 개작, 변형 또는 가공할 수 없습니다.

- 귀하는, 이 저작물의 재이용이나 배포의 경우, 이 저작물에 적용된 이용허락조건을 명확하게 나타내어야 합니다.
- 저작권자로부터 별도의 허가를 받으면 이러한 조건들은 적용되지 않습니다.

저작권법에 따른 이용자의 권리는 위의 내용에 의하여 영향을 받지 않습니다.

이것은 이용허락규약(Legal Code)을 이해하기 쉽게 요약한 것입니다.

Disclaimer

dCollection

공학박사 학위논문

Charging effects on the metals and oxides: *Ab-initio* study

금속 및 산화물의 하전 효과에 대한 제일원리 계산 연구

2021 년 8 월

서울대학교 대학원

재료공학부

박 종 환

Charging effects on the metals and oxides: *Ab-initio* study

지도교수 황 농 문

이 논문을 공학박사 학위논문으로 제출함

2021 년 8월

서울대학교 대학원

재료공학부

박 종 환

박종환의 공학박사 학위논문을 인준함
2021년 8월

위 원 장	김 미 영
부위원장	황 농 문
위 원	한 승 우
위 원	유 병 덕
위 원	권 영 균

Abstract

Using *ab-intio* calculations, the origin of charge enhanced kinetic phenomena in various systems are studied.

To simulate the metals, as a model system, Au(111) slab model is used. When Au(111) is positively charged, the coulomb repulsion generated by surface excess charge. Then the slab thickness expanded to release the residual stress. Because of this expansion, the stacking fault nucleation barrier is decreased. This means the plastic deformation is enhanced by excess positive charging. The effects of vacuum thickness and layer thickness are also investigated.

To simulate the ceramics, as a model system, $\alpha-Al_2O_3$ is used. When the carrier concentration is changed, both for positive and negative charging, the activation barrier, the stacking fault energy, and the required shear stress to create the stacking fault are decreased. Negative charging has bigger effect in the basal slip and positive charging has bigger effect in the pyramidal slip. The difference in GSF energy upon charging in two types of prismatic slips are small compared to that of basal and pyramidal slips.

By using *ab-initio* total-energy and electronic-structure calculations based on the density functional theory, the adsorption and diffusion properties of positively charged Au^+ and negatively charged Au^- adatoms on defect-free MgO(100) surfaces were investigated, in comparison with the case of charge-neutral Au^0 on MgO(100). The most stable adsorption site of Au^+ on MgO(100) is the atop O site, in agreement with that of Au^0, whereas the most stable adsorption site of Au^- on MgO(100) is the atop Mg site. The surface diffusion barrier of Au^+ on MgO(100) is 0.30 eV, larger than that (0.25 eV) of Au^0. For Au^-, the surface diffusion barrier is as low as 0.03 eV. Further detailed analyses of the charge rearrangement, the Bader charges, the electronic structures, and the characteristics of the atomic bonds were also performed. These results exhibit the significant roles of the charge states of Au adatoms in the adsorption and diffusion properties of Au on MgO(100).

By using *ab-initio* calculations, the adsorption and diffusion properties of charged Au dimers (Au_2^+ and Au_2^-) on MgO(100) surfaces were investigated and compared with those of the charge-neutral dimer (Au_2^0) on MgO(100). The most favored adsorption structure of Au_2^+ on MgO(100) is the upright dimer on a surface O atom in agreement with that of Au_2^0. The surface diffusion of Au_2^+ on MgO(100) occurs by the leapfrog process with a barrier height of 0.42 eV lower than that of Au_2^0 (0.69 eV). The most stable adsorption structure of Au_2^- is the flat-lying dimer on two surface Mg atoms. The surface diffusion of Au_2^- can proceed by the hopping and walking processes with the barrier height in the range of 0.10-0.15 eV, which is much lower than the diffusion barriers of Au_2^+ and Au_2^0. Furthermore, detailed information on the electronic structures and charge distribution of Au_2^0, Au_2^+, and Au_2^- are also presented.

Vibrational spectra of charge-neutral and charged Au and Au_2 on MgO(100) were investigated using ab-initio density functional perturbation theory. The calculated vibrational spectra showed vibrational features associated with the charge states of Au and Au_2 on MgO(100). Further analyses of surface in-plane and normal phonon modes of Au and Au_2 on MgO(100) were performed to extract vibrational features involving the Au modes. These features provide important information for experimentally explaining the charge states of Au and Au_2 on MgO(100).

Keyword : metal, oxide, charging, plastic deformation, diffusion
Student Number : 2014-22518

Table of Contents

Chapter 1. Introduction 1

Chapter 2. Charging effects on mechanical property of Au 4

Chapter 3. Charging effects on mechanical property of Al_2O_3 16

Chapter 4. Charging effects on diffusion property of Au monomer on MgO(100) 32

Chapter 5. Charging effects on diffusion of Au dimer on MgO(100) 49

Chapter 6. Charging effects on the vibrational properties of Au and Au_2 on MgO(100) 68

Bibliography 98

Abstract in Korean 101

List of Figures

Figure 2.1 The 7−layer slab used for GSF energy calculation: (from left to right) perfect fcc, one−layer (intrinsic stacking fault, two−layer fault and three−layer (twin) fault. The arrows indicate the successive {111} planes on which Shockley partials with Burgers vector $b_p = \frac{a}{6} < 11\bar{2} >$ are passed.

Figure 2.2 Calculated GSF energy relative to the initial state during slip displacement on {111} planes with different charge densities corresponding to 1.41. 2.81, and 3.52 Å^{-2}.

Figure 2.3 The plane−averaged excess charge density of positively charged Au (111) surface located at the center of supercell.

Figure 2.4 The normal stress acting on Au layers with increasing surface charge density before geometry optimization.

Figure 2.5 The slab thickness of Au(111) with increasing surface charge density after the geometry optimization.

Figure 2.6 Calculated GSF energy relative to the initial state during slip displacement on {111} planes at surface charge density of 2.81 Å^{-2} with different unit cell thickness corresponding to 40.5, 50, and 60Å. The GSF energy decreases as the vacuum thickness increases.

Figure 2.7 Calculated GSF energy relative to the initial state during slip displacement on {111} planes at surface charge density of 2.81 Å^{-2} with different layer thickness corresponding to 7, 10, and 13.

Figure 3.8 Three slip systems of hcp $\alpha-Al_2O_3$: (a) A basal slip, (b) a prismatic slip, and (c) pyramidal slip. The bigger red circles represent O atoms and the smaller gray circles represent Al atoms. The blue, green, and pink plane represents the glide plane of basal, prismatic, and pyramidal slip, respectively.

Figure 3.9 Basal slip: (a) The optimized atomic structures of perfect, unstable stacking fault (γ_{us}), and intrinsic stacking fault (γ_{sf}) during basal slip: (red particles) oxygen, (grey particles) aluminum, (blue line) shear front. (b) Evolution of the system energy during slip along the basal plane with respect to charging.

Figure 3.10 Pyramidal slip: (a) The optimized atomic structures of perfect, and unstable stacking fault (γ_{us}) during pyramidal slip: (red particles) oxygen, (grey particles) aluminum, (blue line) shear front. (b) Evolution of the system energy during slip along the pyramidal plane with respect to charging.

Figure 3.11 Asymmetric prismatic slip: (a) The optimized atomic structures of perfect, unstable stacking fault (γ_{us}), and intrinsic stacking fault (γ_{sf}) during asymmetric prismatic slip: (red particles) oxygen, (grey particles) aluminum, (blue line) shear front. (b) Evolution of the system energy during slip along the asymmetric prismatic plane with respect to charging.

Figure 3.12 Symmetric prismatic slip: (a) The optimized atomic structures of perfect, unstable stacking fault (γ_{us}), and intrinsic stacking fault (γ_{sf}) during symmetric prismatic slip: (red particles) oxygen, (grey particles) aluminum, (blue line) shear front. (b) Evolution of the system energy during slip along the symmetric prismatic plane with respect to charging.

Figure 3.13 Isosurface plots of electron density differences $\Delta\rho^q$ of the geometrically optimized structures of transition states of basal and pyramidal slip system with respect to carrier concentrations. Electron accumulation and depletion regions are denoted in yellow and blue, respectively.

Figure 3.14 TDOSs (black line) and PDOSs of the Al (red lines) and O atoms (green lines) in the perfect [(a), (b), (c), (d), and (e)] and transition state [(f), (g), (h), (i), and (j)] structures of basal slip with respect to carrier concentrations. The energy zero is set to the Fermi energy E_F.

Figure 3.15 TDOSs (black line) and PDOSs of the Al (red lines) and O atoms (green lines) in the perfect [(a), (b), (c), (d), and (e)] and transition state [(f), (g), (h), (i), and (j)] structures of pyramidal slip with respect to carrier concentrations. The energy zero is set to the Fermi energy E_F.

Figure 4.16 Top views of the adsorption structures of Au adatoms on MgO(100) surfaces: adsorption (a) on top of a surface O site, (b) in a surface hollow site (H), and (c) on top of a surface Mg site. The $p(3\times3)$ surface unit cell used in the calculations is denoted by black lines.

Figure 4.17 Isosurface plots of electron density differences $\Delta\rho^q$ superimposed on side views of the geometrically optimized structures if the charged Au adatoms at the three adsorption sites on MgO(100). Electron accumulation and depletion regions are denoted in yellow and blue, respectively. The isosurface levels are ±0:003 electrons/bohr^3.

Figure 4.18 Side views of the geometrically optimized atomic structures of the charge−neutral and charged Au adatoms at the three adsorption sites on MgO(100). The numbers represent Bader charges (in units of $|\boldsymbol{e}|$) of Au and its neighboring surface atoms.

Figure 4.19 PDOSs of the Au (shaded) and MgO atoms (black lines) in the top two MgO layers for the charge−neutral and charged Au adatoms at the three adsorption sites on MgO(100). The energy zero is set to the Fermi energy E_F. It is herein noted that the PDOS peaks in the band gap region of MgO consist of hybrid states of Au and the surface atoms of MgO(100).

Figure 4.20 Projected crystal orbital Hamilton population analysis of atomic bonds during the adsorption of charge−neutral and charged Au adatoms at the three adsorption sites on MgO(100) surfaces. The energy zero is set to the Fermi energy E_F.

Figure 5.21 Top and side views of the adsorption structures of Au dimers on MgO(100): (a) the upright dimer on an O site (S_{O}), (b) the upright dimer on a H site (S_{H}), (c) the flat−lying dimer on two O sites ($P_{O\text{-}H\text{-}O}$), (d) the flat−lying dimer on two Mg sites ($P_{Mg\text{-}H\text{-}Mg}$), (e) the flat−lying dimer on two H sites with an O atom at the dimer bond center ($P_{H\text{-}O\text{-}H}$), and (f) the flat−lying dimer on two H sites with a Mg atom at the dimer bond center ($P_{H\text{-}Mg\text{-}H}$).

Figure 5.22 Energy profiles of the Au dimers diffusing by the indicated atomic processes on MgO(100), calculated within the CI−NEB.

Figure 5.23 Projected spin−polarized electronic densities of states (PDOSs) of the Au dimer atoms and the MgO atoms in the top two MgO layers for the charge−neutral and charged Au dimers at the three stable adsorption sites on MgO(100). The energy zero is set to the Fermi energy E_F.

Figure 5.24 Isosurface plots of electron density differences $\Delta \rho q$ superimposed on the side views of the geometry−optimized structures of the three adsorption configurations for each charge state of the charged Au dimer on MgO(100). Electron accumulation and depletion regions are denoted by yellow and blue, respectively. The isosurface levels are ±0.002 electrons/bohr^3.

Figure 6.25 Top view of clean MgO(100) and side views of the geometry−optimized adsorption structures of the charge−neutral and charged Au adatoms on MgO(100): (a) Clean MgO(100), (b) Au^0 on top of a surface O atom of MgO(100), (c) Au$^+$ on top of a surface O atom of MgO(100), and (d) Au$^-$ on top of a surface Mg atom of MgO(100). The black lines in (a) denote the 3×3 surface unit cell used in the calculations.

Figure 6.26 Calculated surface phonon densities of states (ph−DOSs) of clean MgO(100) and Au^q (q = 0, +, −) on MgO(100): (a) Clean MgO(100), (b) Au^0 , (c) Au$^+$, and (d) Au$^-$. The black lines represent the surface ph−DOSs of clean MgO(100) and Au^q on MgO(100). Here, the phonon spectra of clean MgO(100) are the projected ph−DOSs of the two upper MgO−layer atoms (Mg and O), whereas the phonon spectra of Auq on MgO(100) also include the adsorbed Au adatoms. The green and blue lines represent the Mg− and O−projected vibrational modes of the two topmost MgO−layer atoms, respectively. The red line represents the Au−projected vibrational modes. In the calculations, the phonon eigenvalues were broadened using a Gaussian function of width 0.4 THz.

Figure 6.27 Enlarged ph−DOs bands in the region below 5 THz for Au^q (q = 0, +, −) on MgO(100): (a) Au^0, (b) Au$^+$, and (c) Au$^-$. The black solid line represents the projected ph−DOSs of the two upper MgO−layer atoms (Mg and O atoms) and adsorbed Au atoms. The orange and the purple lines represent the surface in−plane and the surface normal vibrational modes of the adsorbed Au atoms, respectively. In the calculations, the phonon eigenvalues were broadened using a Gaussian function of width 0.4 THz.

Figure 6.28 Representations of the surface in−plane [(a), (c), and, (e)] and the surface normal [(b), (d), and (f)] phonon modes for the most stable adsorption structures of Au^q on MgO(100) structures, corresponding to the selected frequencies in Table 1. Blue arrows indicate the amplitude and direction for each atom in each phonon mode. (a) Frustrated translation−1 mode of Au^0 (b) Stretching−1 mode of Au^0 , (c) Frustrated translation−1 mode of Au$^+$, (d) Stretching−1 of Au$^+$, (e) Frustrated translation−2 mode of Au$^-$, and (f) Stretching−2 of Au$^-$. The numbers for Au^0 and Au$^+$ (Au$^-$) on MgO(100) represent the interatomic distances between O$_s$ (Mg$_s$) and its neighboring atoms in Å.

Figure 6.29 Side views of the geometry−optimized adsorption structures of Au$_2^q$ on MgO(100): (a) Upright Au$_2^0$ (Au$_2^0$ −S_O), (b) upright Au$_2^+$ (Au$_2^+$−S_O) on top of a surface O atom of MgO(100), and (c) flat−lying Au$_2^-$ (Au$_2^-$ −$P_{\text{Mg−H−Mg}}$) on top of two surface Mg atoms of MgO(100).

Figure 6.30 Calculated ph−DOSs of Au$_2^q$ (q = 0, +, −) on MgO(100): (a) Au$_2^0$ −S_O, (b) Au$_2^+$−S_O, and (c) Au$_2^-$ −$P_{\text{Mg−H−Mg}}$. The black line represents the surface ph−DOSs of Au$_2^q$ on MgO(100). Here, the phonon spectra of Au$_2^q$ on MgO(100) also show the projected ph−DOSs of the two upper MgO−layer atoms (Mg and O) and adsorbed Au$_2$ atoms. The green and blue lines represent the Mg− and O−projected vibrational modes of the two topmost MgO−layer atoms, respectively. The red line represents the vibrational modes of adsorbed Au2 atoms. In the calculations, the phonon eigenvalues were broadened using a Gaussian function of width 0.4 THz.

Figure 6.31 Enlarged ph−DOSs bands in the region below 8 THz for Au_2^q (q = 0, +, −) on MgO(100): (a) Au_2^0 -S_O, (b) Au_2^+-S_O, and (c) Au_2^- -$P_{Mg-H-Mg}$. The black solid line represents the projected ph−DOSs of the two upper MgO−layer atoms (Mg and O) and adsorbed Au2 atoms. The orange and the purple lines represent the surface in−plane and the surface normal vibrational modes of the adsorbed Au_2 atoms, respectively. In the calculations, the phonon eigenvalues were broadened using a Gaussian function of width 0.4 THz.

Figure 6.32 Representations of the surface in−plane [(a), (b), (e), (f), (i), (j), (k), and (l)] and the surface normal [(c), (d), (g), (h), (m), and (n)] phonon modes for the most stable adsorption structures of Au_2^q on MgO(100), corresponding to the selected frequencies in Table 2. Arrows indicate the amplitude and direction for each atom in each phonon mode. (a) Frustrated translation of Au_2^0, (b) frustrated rotation of Au_2^0, (c) stretching−3 of Au_2^0, (d) stretching−4 of Au_2^0, (e) frustrated translation of Au_2^+, (f) frustrated rotation of Au_2^+, (g) stretching−3 of Au_2^+, (h) stretching−4 of Au_2^+, (i) frustrated rotation−z of Au_2^-, (j) frustrated translation−y of Au_2^-, (k) frustrated translation−x of Au Au_2^-, (l) stretching−x of Au_2^-. (m) frustrated rotation−y of Au_2^-, and (n) stretching−z of Au_2^-. The numbers for Au_2^0 and Au_2^+ on MgO(100) represent the interatomic distances between O_s and its neighboring atoms in Å.

List of Tables

Table 2.1 The calculated 6 specific points of GSF energies with surface charge densities of +1.41. +2.81, and +3.52 $Å^{-2}$

Table 4.1 Calculation results for the physical properties of the charge−neutral and charged Au adatoms at the three adsorption sites on MgO(100): interatomic distance d of Au with the neighboring atoms and energy ΔE relative to that of the most stable adsorption site.

Table 5.1 Calculation results for the adsorption properties of the charge−neutral and charged Au dimers at the three stable adsorption sites on MgO(100): total energy ΔE relative to that of the most stable adsorption structure, interatomic distance d, and total magnetic moment μ.

Table 5.2 Calculation results for the diffusion processes and barriers of the charge−neutral and charged Au dimers (Au_2^0, Au_2^+, and Au_2^-) on MgO(100).

Table 5.3 Calculation results for the diffusion processes and barriers of the charge−neutral and charged Au dimers (Au_2^0, Au_2^+, and Au_2^-) on MgO(100).

Table 6.1 Calculated frequencies and corresponding representations of surface phonon modes for the most stable adsorption structures of Au^q (q=0, +, −) on MgO(100).

Table 6.2 Calculated frequencies and corresponding representations of surface phonon modes for the most stable adsorption structures of Au_2^q (q = 0, +, −) on MgO(100).

Chapter 1. Introduction

1.1. Charge enhanced kinetic

Lately, there has been increasing interest in the effect of electric charges in the material sciences [1-9].

In metallic materials, kinetic enhancement due to the charging effect compared to the charge-neutral state has been reported. The improved elongation by applied electric current was reported during tensile test in various metallic materials [10-15]. This phenomenon is called electro-plasticity. Electro-pulsing treatment efficiently enhanced the recrystallization kinetics in interstitial free steel and AZ31 magnesium alloy [16]. In the plasma-assisted annealing of as-cold rolled Fe-1% steel, the recrystallization accelerated by the accumulated charge on the insulating substrate compared to conducting substrate [17]. The dewetting kinetics of as-deposited metal thin films also enhanced because of charge build-up on the insulating substrate in plasma treatment [18,19]. Oxide-supported metal nanoparticles continuously change their structures under e-beam irradiation during in-situ transmission electron microscopy (TEM) observation in less than a second. In this structural fluctuation, metal nanoparticles are forming multiply twinned particles or stacking disorders accompany by shear deformation [20,21]. Structure instability observed not only in oxide but also in metal particles mounted on other insulating substrates. However, the continuous structural change of metal particles is not observed in the conducting substrate. In addition, the coalescence of two metal particles on the insulating substrate is also completed significantly faster than on the conductive substrate [22].

In ceramic materials, although their high hardness, high heat resistance, and high chemical stability, the commercial application is limited due to their difficulties in processing. As one of the new process variables, research on the effect of charging on the mechanical properties of ceramic materials is being actively conducted. Electron-beam-induced superplastic compression and elongation of amorphous silica were discovered using in-situ TEM observation [4]. A similar phenomenon was discovered in the experiment comparing the elongation of Li_2O nanowires with and without e-beam irradiation [3]. Electric-field-induced improvement in elongations were reported in Al_2O_3 and 3Y-TZP [23,24]. Using the theoretical method, the effect of charging on the mechanical properties of the Ⅱ-Ⅵ ionic compound (ZnS, ZnTe, and CdTe) was studied with respect to carrier concentration. The excess electrons (holes) catalyze the plastic deformation of ceramic materials by decreasing the activation energy of slip displacement [9].

1.2. Properties and applications of metal/oxide.

Metal nanoparticles and thin films are attracting a lot of attention because of their wide range of technological applications such as heterogeneous catalysis, gas sensors, corrosion−protective coatings, medical implants, photovoltaic devices, and microelectronic devices [25−46]. The charge state of metal/oxide systems has a decisive effect on their catalytic activity and atomic structure [26−28,47−57] . Therefore, understanding the charging effects on the adsorption and diffusion properties of the metal/oxide system is indispensable for constructing the desired catalytic design.

Chapter 2. Charging effects on mechanical property of Au

2.1. Introduction

Recently, there has been increasing experimental evidence of the importance of electrical charging in the material manufacturing processes such as diffusion, recrystallization and deformation [1−9]. Especially for metallic materials, enhanced kinetic behaviors were observed in charged metal systems compared with that in charge−neutral metal systems. The elongation during deformation can be drastically increased under the electric current compared to that without the electric current in various metallic materials [10−15]. Kim et al. explained the origin of these electro−plasticity of metallic materials that charge imbalance near the defect softens the bonding using ab−initio calculation, finite element simulations, and experimental results [58].

The recrystallization kinetics can be enhanced by electro−pulsing treatment by the athermal effect distinct from joule heating in interstitial free steel and AZ31 magnesium alloy [16]. During plasma treatment, the recrystallization kinetics are enhanced by the charge buildup on the insulating substrate compared to conducting substrate without charge buildup in Fe−1%Si steel [18].

In comparing the microstructures of Sn and Au thin films on the insulating and conducting substrates after plasma treatment, the accelerated dewetting kinetics is observed on the insulating substrate by charge buildup than on the conducting substrate without charge buildup [18,19].

Oxide−supported Au nanoparticles had structural instability under electron irradiations that are constantly changing their structures and are forming stacking disorders or twinning caused by shear deformation at a fraction of a second during in−situ transmission electron microscopy(TEM) observation [20,21].

Concerning these phenomena, Kim compared the behaviors of Au nanoparticles on the insulating and conducting substrates [22]. Au nanoparticles on the insulating substrate showed dynamic behaviors such as rapid orientation change and accelerated coalescence, whereas Au nanoparticles on the conducting substrate showed sluggish behavior with no orientation change and slow coalescence.

Despite these studies, the origin of this charge enhanced kinetic remains uncertain. The purpose of this study is to investigate the charging effects on metals by using DFT calculation. The charge dependent mechanical properties of Au by investigated generalized−stacking fault (GSF) energy calculation is performed. To modify the slip systems of Au with and without charge, we used the slab model of Au(111) surface, which is the slip plane of FCC. The calculation showed significant roles of charging on slip processes, which is a crucial factor in understanding charge dependent mechanical properties of metals.

2.2. Computational Details

All calculations were performed using the spin-polarized DFT as implemented in the cod of the Vienna *Ab-intio* Simulation Package (VASP) [59,60]. The generalized gradient approximation (GGA) functional of Perdew-Burke-Ernzerhof (PBE) [61] was used to describe the exchange-correlation interactions combined with a projector-augmented wave (PAW) method [62]. The (111) surface of the Au was simulated by a repeating slab model consisting of 7 atomic Au layers and a 26.5 Å vacuum region. Plane waves with an energy cutoff of 300 eV were used to describe the electronic wave functions. The **k**-space integration was performed using a 8 × 8 uniform grid in the surface Brillouin zone (SBZ) of the surface unit cell. The geometry was optimized until the remaining atomic forces were smaller than 0.01 eV/Å. For generalized stacking fault energy calculation, a slab model in which parts of atomic layers were rigidly translated by a displacement toward a specific direction on a particular lattice plane is usually constructed. A perfect dislocation with Burgers vector dissociates into two Shockley partial dislocations.

2.3. Results and Discussion

For the bulk fcc metals, Kibey et al., studied the twin nucleation energy and twin boundary energy in GSF energy curves using 12-layer slab model with atomic constrain in z-direction to modify the bulk system [63]. Here, we carried out the GSF energy calculation using 7-layer slab model without constrain in z-direction to modify the nano particles and thin films. The Burgers vector of perfect dislocation can be divided into the Burgers vectors of two Shockley partial dislocations with the same energy,

$$\frac{1}{2} < \bar{1}10 > \ \rightarrow \ \frac{1}{6} < \bar{2}11 > \ + \ \frac{1}{6} < \bar{1}2\bar{1} >.$$

The obtained GSF energy of Au are shown as black lines in Fig. 2. 2. In the displacement pathway along Burgers vector, there exist three local maxima(γ_{us1}, γ_{us2}, and γ_{us3}) and three local minima(γ_{sf1}, γ_{sf2}, and γ_{sf3}): (1) The unstable stacking fault energy, γ_{us1}, which means the energy barrier of intrinsic stacking fault nucleation, (2) the intrinsic stacking fault energy, γ_{sf1}, (3) The unstable stacking fault energy, γ_{us2}, which means the energy barrier of twin nucleation,

(4) the two layer twin boundary energy, γ_{sf2}, (5) the unstable stacking fault energy, γ_{us3}, which means the energy barrier of perfect twin nucleation, (6) the perfect twin boundary energy, γ_{sf3}.

To investigate the charging effects on the mechanical properties of Au, we examined the GSF energy with charging along slip paths that is . To examine the charging effects, we extracted 0.2, 0.4, and 0.5 electrons per unit cell to simulate positive charging to the supercell, corresponding to the surface charge density of +1.41. +2.81, and +3.52 Å^{-2}, respectively. The calculation results of six specific points with positive charging are summarized in Tab. 2. 1.

For the neutral case, the unstable stacking fault energies of γ_{us1}, γ_{us2}, and γ_{us3} are 6.71, 8.04, and 8.30 meV/Å^2, respectively. The values of these results are slightly decreased compared to the results in [63]. In this study, we optimized the slab model in z-direction to modify the nanostructures, so the stress along the z-direction is released compared to the results in [63]. The stacking fault energies of γ_{sf1}, γ_{sf2}, and γ_{sf3} are 4.06, 3.96, and 2.44 meV/Å^2, respectively.

For the positive charged surface with surface charge density of 1.41 Å^{-2}, the unstable stacking fault energies of γ_{us1}, γ_{us2}, and γ_{us3} are 7.09, 8.28, and 8.52 meV/Å^2, respectively. The unstable stacking fault energies are slightly increased by ~0.2 meV/Å^2 approximately. The stacking fault energies of γ_{sf1}, γ_{sf2}, and γ_{sf3} are 4.49, 4.47, and

2.77 meV/Å^2, respectively. The stacking fault energies are slightly increased by ~0.4 meV/Å^2 approximately.

For the positive charged surface with surface charge density of 2.81 Å^{-2}, the unstable stacking fault energies of γ_{us1}, γ_{us2}, and γ_{us3} are 5.71, 6.72, and 7.13 meV/Å^2, respectively. The unstable stacking fault energies are slightly decreased by ~1.4 meV/Å^2 approximately. The stacking fault energies of γ_{sf1}, γ_{sf2}, and γ_{sf3} are 3.83, 4.00, and 2.50 meV/Å^2, respectively. The stacking fault energies are almost same with that of the neutral surface.

For the positive charged surface with surface charge density of 3.52 Å^{-2}, the unstable stacking fault energies of γ_{us1}, γ_{us2}, and γ_{us3} are 4.76, 5.50, and 5.84 meV/Å^2, respectively. The unstable stacking fault energies are slightly decreased by ~2.5 meV/Å^2 approximately. The stacking fault energies of γ_{sf1}, γ_{sf2}, and γ_{sf3} are 2.99, 3.25, and 1.98 meV/Å^2, respectively. The stacking fault energies are slightly increased by ~0.7 meV/Å^2 approximately.

In Fig. 3.3, we present the plane-averaged excess charge densities of the positive charged slab along the z-direction with increasing charge densities of 1.41. 2.81, and 3.52 Å^{-2}. The excess charges are obtained from the difference between the charged slab and neutral slab frozen to the geometry of the charged slab. The excess positive charge located mostly on the outmost Au layers in the vacuum region. The excess charge densities are increasing as the number of charge increasing.

In Fig 2.4 and 2.5, we present the normal stress acting on the Au layers before the geometry optimization and slab thickness after the geometry optimization with increasing charge densities of 1.41. 2.81, and 3.52 $Å^{-2}$. Fig. 2.4 show that because of the positive charge accumulation on the outmost Au layer, the coulomb repulsion increasing as charge density increasing. So the surface normal stress acting on the outmost layer (black line in Fig.4.a) increasing as the charge density increasing. Because of this stress change by excess positive charge, Fig. 2.5 show that the slab thickness is increasing as the charge density.

To investigate the effect of vacuum thickness, we compared the GSF energy in the same charge state with increasing vacuum thickness. Fig. 2.6 represents the GSF energy difference in surface charge density of +2.81 $Å^{-2}$ with an increasing unit cell thickness of 40.5, 50, and 60 that contain vacuum and Au 7-layers. The GSF energy decreases as the vacuum thickness increases. The reason is that as the vacuum thickness increases, more excess charge is transferred from the inside to the outside of the surface [64].

To investigate the effect of layer thickness, we compared the GSF energy in same charge state with increasing layer thickness with same vacuum thickness of 26.5 Å before relaxation. Fig. 2.7 represents the GSF energy difference in surface charge density of +2.81 $Å^{-2}$ with an increasing layer thickness of 7, 10, and 13. The 10-layer surface has the highest GSF energy, which seems to be the even-odd effect. As the thickness increases from 7 to 11 layers, the GSF energy decreases because the distance between excess charges increases due to increased thickness.

2.4. Conclusion

In this paper, we use DFT to calculate the (111) GSF surfaces of charge-neutral and charge Au. The GSF calculation finds that the excess positive charge decrease the energy barrier of stacking fault nucleation. This results show that plastic deformation enhanced by excess positive charge. The reason is that the outmost layer repulse each other because the accumulated positive charge increases the coulomb repulsion force. The results can also provide physical and chemical insights into an understanding of microscopic mechanisms underlying the charge-dependent kinetics such as structure instability, dewetting, and recrystallization of charged metal nanoparticles on insulators.

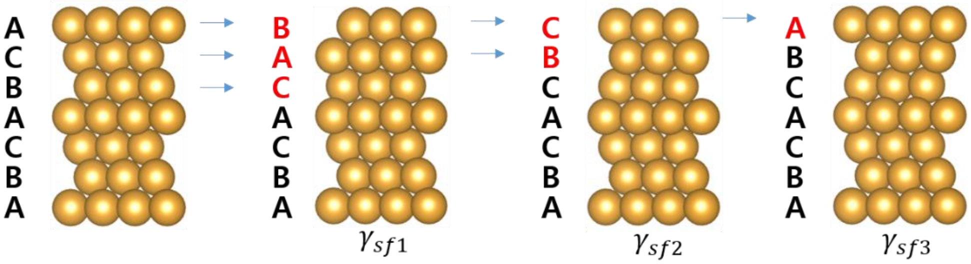
A
C
B
A
C
B
A
B
A
C
A
C
B
A
γ_{sf1}
C
B
C
A
C
B
A
γ_{sf2}
A
B
C
A
C
B
A
γ_{sf3}

Figure 2.1 The 7−layer slab used for GSF energy calculation: (from left to right) perfect fcc, one−layer (intrinsic stacking fault, two−layer fault and three−layer (twin) fault. The arrows indicate the successive {111} planes on which Shockley partials with Burgers vector $b_p = \frac{a}{6} < 11\bar{2} >$ are passed.

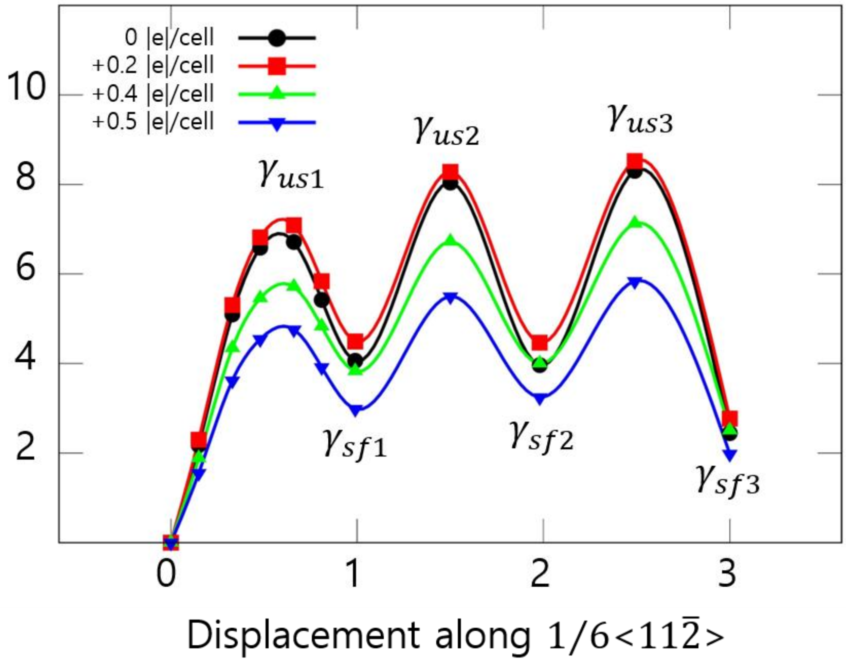

Figure 2.2 Calculated GSF energy relative to the initial state during slip displacement on {111} planes with different charge densities corresponding to 1.41. 2.81, and 3.52 Å^{-2}.

Table 2.1 The calculated 6 specific point of GSF energies with surface charge densities of +1.41. +2.81, and +3.52 $Å^{-2}$.

Charge	γ_{us1}	γ_{us2}	γ_{us3}	γ_{sf1}	γ_{sf2}	γ_{sf3}
[$Å^{-2}$]	[$meV/Å^2$]					
0	6.71	8.04	8.30	4.06	3.96	2.44
+1.41	7.09	8.28	8.52	4.49	4.47	2.77
+2.81	5.71	6.72	7.13	3.83	4.00	2.50
+3.52	4.76	5.50	5.84	2.99	3.25	1.98

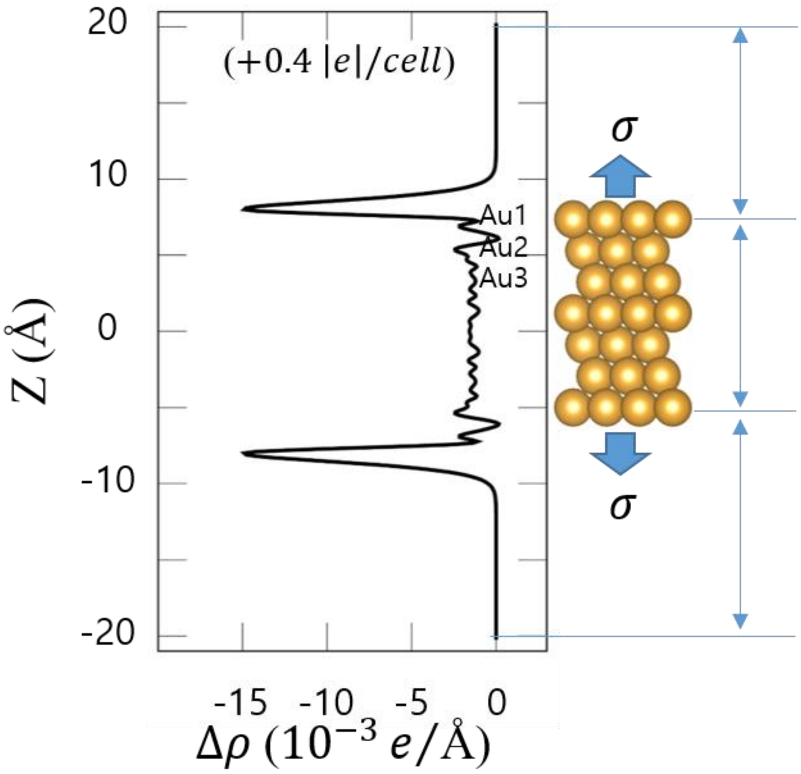

Figure 2.3 The plane-averaged excess charge density of positively charged Au (111) surface located at the center of supercell.

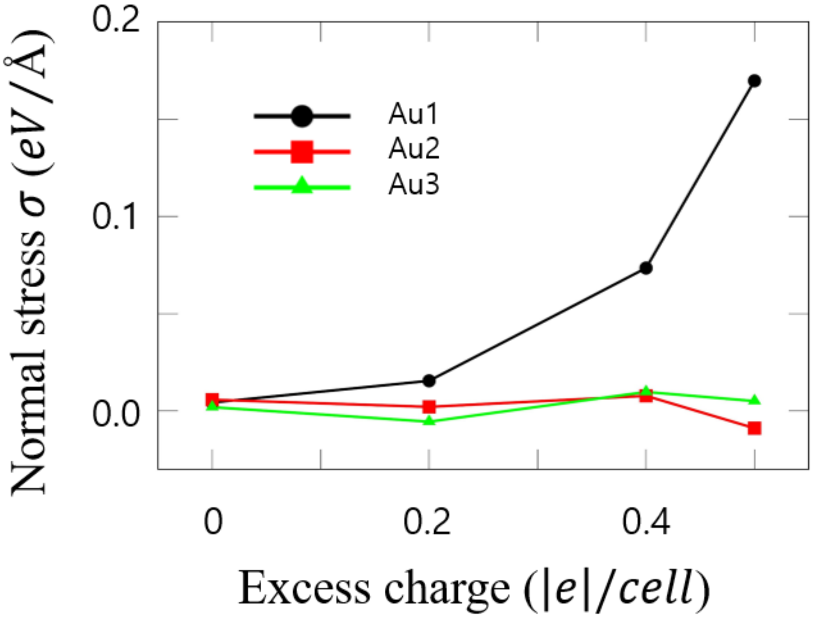

Figure 2.4 The normal stress acting on Au layers with increasing surface charge density before geometry optimization.

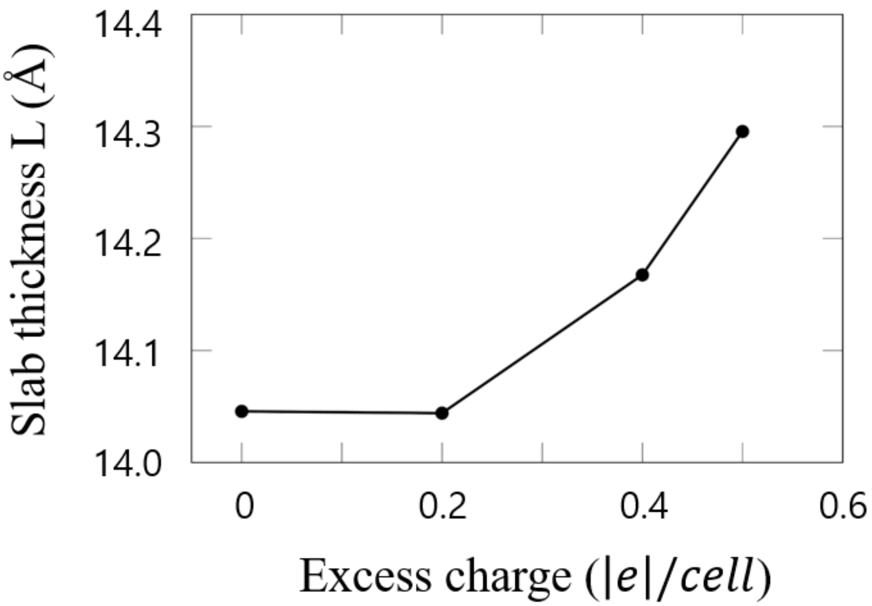

Figure 2.5 The slab thickness of Au(111) with increasing surface charge density after the geometry optimization.

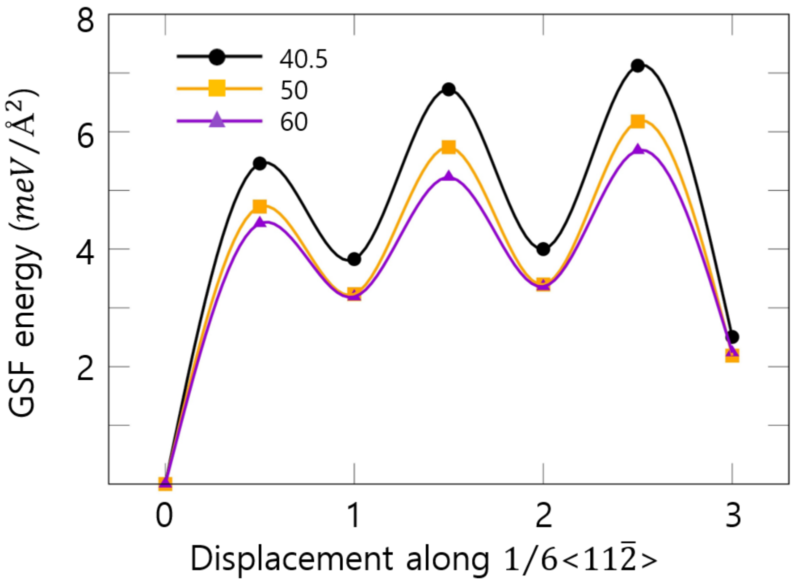

Figure 2.6 Calculated GSF energy relative to the initial state during slip displacement on {111} planes at surface charge density of 2.81 $Å^{-2}$ with different unit cell thickness corresponding to 40.5, 50, and 60 Å. The GSF energy decreases as the vacuum thickness increases.

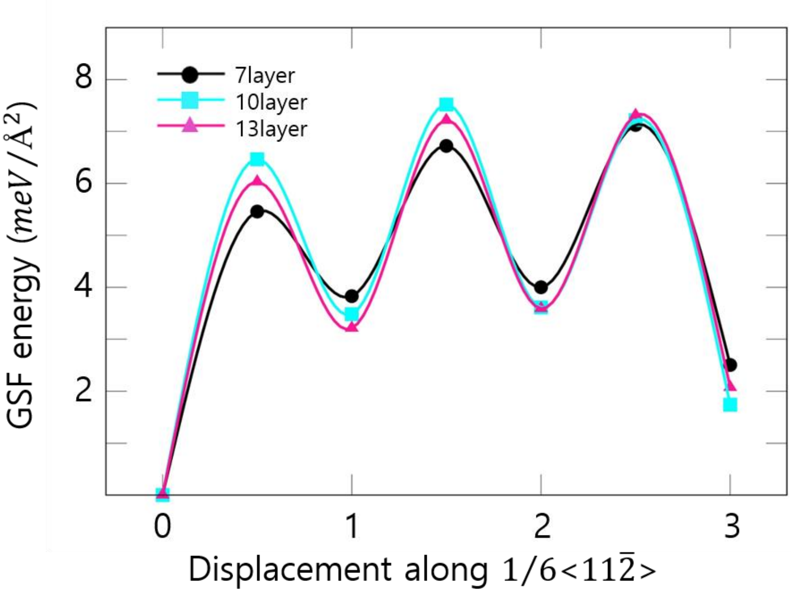

Figure 2.7 Calculated GSF energy relative to the initial state during slip displacement on {111} planes at surface charge density of 2.81 $Å^{-2}$ with different layer thickness corresponding to 7, 10, and 13.

Chapter 3. Charging effects on mechanical property of Al_2O_3

3.1. Introduction

Recently, various studies have reported on the charging effects on material processing [1-9]. Especially for ceramic materials, controlling their mechanical properties is very important for commercial applications because of their high brittleness and low fracture toughness. Zheng et al. reported that electron-beam irradiation could induce superplastic deformation of amorphous silica using in-situ compression and tensile tests inside transmission electron microscopy [4]. Zheng et al. observed super-elongation of the polycrystalline Li_2O nanowires under electron beam irradiation compared with that without e-beam irradiation using in-situ TEM observation during tensile tests [3]. For the bulk ceramic materials, elongation increases under electrical field compared to without the e-field using fine-grained Al2O3 and 3Y-TZP specimens [23,24].

Shen et al. found that the mechanical properties of the ionic semiconductor material such as ZnS, ZnTe, and CdTe can change by carrier concentration (electron or hole) using density functional theory (DFT) calculation. Electron (or hole) carriers reduced generalized stacking fault (GSF) energy, representing the formation barrier of the stacking fault or twin boundary [9].

Despite these studies, the charging effects on the mechanical properties of oxide materials remain unidentified. The purpose of this study is to investigate the charging effects on oxides by using DFT calculation. As a model system to examine the charging effect on ceramics, we herein consider Al_2O_3, of which both experimental and theoretical methods have widely studied about a charge-neutral system [65-72]. There are three crucial slip systems that are forming the dislocations and twins in sapphire: basal, pyramidal, and prismatic slips. The charge-dependent mechanical properties of Al2O3 by investigating generalized-stacking fault (GSF) energy calculation for three slip systems are performed. To simulate the mechanical properties of Al_2O_3 upon charging, we inject (or extract) electrons to the periodic bulk Al_2O_3 lattice without vacuum space.

3.2. Computational Details

All calculations were performed using the spin-polarized DFT as implemented in the cod of the Vienna *Ab-intio* Simulation Package (VASP) [59,60]. The generalized gradient approximation (GGA) functional of Perdew-Burke-Ernzerhof (PBE) [61] was used to describe the exchange-correlation interactions combined with a projector−augmented wave (PAW) method [54,62]. Plane waves with an energy cutoff of 450 eV were used to describe the electronic wave functions. The **k**−space integration was performed using a 3 × 3 uniform grid in the surface Brillouin zone (SBZ) of the surface unit cell. The geometry was optimized until the remaining atomic forces were smaller than 0.01 eV/Å. To calculated the GSF energy, we constructed a supercell with certain crystallographic directions (depending on the slip system to be studied) in which parts of atomic layers were rigidly translated by a displacement toward a specific direction on a particular lattice plane is usually constructed.

To simulate the change of carrier concentration, we added one or two electrons to obtain a high electron concentration while removing one or two electrons to obtain a high hale concentration.

3.3. Results and Discussion

In order to obtain a reasonable slip deformation path, we considered following four possible slip paths in the GSF energy calculation: (1) Basal slip along $\{0001\} < \overline{1}\overline{1}20 >$, (2) pyramidal slip along $\{01\overline{1}2\} < 0\overline{1}11 >$, (3) asymmetric prismatic slip along $\{1\overline{2}10\} < 01\overline{1}0 >$ while slice the $\{1\overline{2}10\}$ plane between Al and O layers, and (4) symmetric prismatic slip along $\{1\overline{2}10\} < 01\overline{1}0 >$ while slice the $\{1\overline{2}10\}$ plane between two Al layers. The obtained GSF energy of neutral Al_2O_3 for each slip systems are shown as black lines in Fig 3.(2-5) (b). There are two specific points on γ-surface determining the deformation mechanism of Al_2O_3: (1) The unstable stacking fault (USF) energy, γ_{us}, located at $\frac{2}{9}<0\bar{1}10>$ for basal, $\frac{1}{6}<0\bar{1}11>$ for pyramidal, $\frac{1}{6}<0\bar{1}10>$ for two prismatic slip systems, (2) the intrinsic stacking fault energy γ_{isf}, located at $\frac{1}{3}<0\bar{1}10>$ for basal, $\frac{1}{6}<0\bar{1}10>$ for two prismatic slip systems.

To investigate the charging effects on the mechanical properties of Al_2O_3, we examined the GSF energy with charging along all 4 plausible slip paths. To examine the charging effects, we added(negative) and extracted(positive) one and two electrons to the supercell of 90 atoms, corresponding to the carrier concentration of $\pm 6.38 \times 10^{20}$ cm^{-3} and $\pm 12.76 \times 10^{20}$ cm^{-3}, respectively.

In HCP materials, basal slip is the most frequently occurring plastic deformation mechanism. In the basal slip model suggested in [], the slip plane appears in the middle of the two Al layers that separate the Al_2O_3 crystal into two blocks. The Burgers vector of perfect dislocation of basal slip can be divided into the Burgers vectors of two energetically favorable partial dislocations with,

$$\frac{1}{3}<\overline{11}20> \rightarrow \frac{1}{3}<\bar{1}010> + \frac{1}{3}<0\bar{1}10> .$$

Because the energy of the two partial slips is identical, we only consider one of a partial dislocation displacement along the Burgers vector to obtain the parameters of the basal slip. Despite the same energy, a possible dislocation direction is constrained to one of these two partial directions. It is impossible in dislocation movement in the other direction because the two Al atoms opposing on the slip plane become too close increasing electrostatic energy.

Fig. 3.2 (a) shows the atomic structures after optimization of perfect, unstable stacking fault (γ_{us}), and intrinsic stacking fault (γ_{sf}) during basal slip along $\frac{1}{3} < 0\bar{1}10 >$. Fig. 3.2 (b) represents the evolution of the system energy difference relative to the initial state during basal slip upon charging.

As shown in Fig. 3.2 (b), adding electrons significantly decrease the GSF energy of the neutral system. For the carrier concentration of 6.38×10^{20} cm^{-3}, the γ_{us} decreases from 111.24 to 105.64 eV/Å^2, which is 4.50 % decreased. γ_{isf} also slightly decreases from 88.50 to 84.65 eV/Å^2. For the carrier concentration of 12.76×10^{20} cm^{-3}, the γ_{us} decreases from 111.24 to 87.56 eV/Å^2, which is 21.29 % decreased. γ_{isf} also slightly decreases from 88.50 to 80.47 eV/Å^2. The calculated shear stress required to create stacking fault for carrier concentration of 0 cm^{-3}, 6.38×10^{20} cm^{-3} and 12.76×10^{20} cm^{-3} are 12.87, 12.22, and 10.13 GPa, respectively

In the case of positive charging, as shown in Fig. 3.2 (b), removing electrons decrease the GSF energy of the neutral system, but the effects is less than negative charging. For the carrier concentration of 6.38 × 10^{20} cm^{-3}, the γ_{us} decreases from 111.24 to 104.45 eV/$Å^2$, which is 6.10 % decreased. γ_{isf} also slightly decreases from 88.50 to 86.68 eV/$Å^2$. For the carrier concentration of 12.76 × 10^{20} cm^{-3}, the γ_{us} decreases from 111.24 to 98.55 eV/$Å^2$, which is 11.41 % decreased. γ_{isf} also slightly decreases from 88.50 to 80.47 eV/$Å^2$. The calculated shear stress required to create stacking fault for carrier concentration of 0 cm^{-3}, 6.38 × 10^{20} cm^{-3} and 12.76 × 10^{20} cm^{-3} are 12.87, 12.08, and 11.40 GPa, respectively

Pyramidal slip is the only dislocation system that has [0001] component in its Burgers vector. There are several possible Burgers vectors in pyramidal dislocations, and the $\frac{1}{3}[0\bar{1}11]$ direction is most beneficial energetically. Fig. 3.3 (a) shows the atomic structures after optimization of perfect, and unstable stacking fault (γ_{us}) during pyramidal slip along $\frac{1}{3}[0\bar{1}11]$. Fig. 3.3 (b) represents the evolution of the system energy difference relative to the initial state during pyramidal slip upon charging.

As shown in Fig 3.3 (b), adding electrons significantly decrease the GSF energy of the neutral system. For the carrier concentration of 6.38 × 10^{20} cm^{-3}, the γ_{us} decreases from 223.34 to 214.03 eV/$Å^2$, which is 4.17 % decreased. For the carrier concentration of 12.76

$\times\ 10^{20}$ cm^{-3}, the γ_{us} decreases from 223.34 to 204.14 eV/Å^2, which is 8.60 % decreased. The calculated shear stress required to create stacking fault for carrier concentration of 0 cm^{-3}, 6.38 $\times\ 10^{20}$ cm^{-3} and 12.76 $\times\ 10^{20}$ cm^{-3} are 13.84, 13.27, and 12.65 GPa, respectively.

In the case of positive charging, as shown in Fig. 3.3. (b), removing electrons decrease the GSF energy of the neutral system, but the effect is stronger than negative charging. For the carrier concentration of 6.38 $\times\ 10^{20}$ cm^{-3}, the γ_{us} decreases from 223.34 to 203.58 eV/Å^2, which is 8.85 % decreased. For the carrier concentration of 12.76 $\times\ 10^{20}$ cm^{-3}, the γ_{us} decreases from 223.34 to 186.91 eV/Å^2, which is 16.31 % decreased. The calculated shear stress required to create stacking fault for carrier concentration of 0 cm^{-3}, 6.38 $\times\ 10^{20}$ cm^{-3} and 12.76 $\times\ 10^{20}$ cm^{-3} are 13.84, 12.62, and 11.58 GPa, respectively.

Prismatic slip system is the dominant slip mechanism at low temperature [73]. The Burgers vector of perfect dislocation of prismatic slip can be divided into the Burgers vectors of three energetically favorable partial dislocations,

$$< 01\bar{1}0 > \rightarrow \frac{1}{3} < 01\bar{1}0 > + \frac{1}{3} < 01\bar{1}0 > + \frac{1}{3} < 01\bar{1}0 >,$$

with sequential generation of stacking faults. In this study, two prismatic slips were considered according to the position of the slip plane. First is asymmetric prismatic slip that slip plane is located between the Au and O layers as shown in Fig. 3. 4(a). Second is symmetric prismatic slip that slip plane is located between the two O layers as shown in Fig. 3. 5(a).

Fig. 3.4 (a) shows the atomic structures after optimization of perfect, unstable stacking fault (γ_{us}), and intrinsic stacking fault (γ_{sf}) during asymmetric prismatic slip along $\frac{1}{3} < 0\bar{1}10 >$. Fig. 3.4 (b) represents the evolution of the system energy difference relative to the initial state during asymmetric prismatic slip upon charging.

For the asymmetric prismatic slip, the slip lane slices the bond between Al and O layers. In the case of negative charging, for the carrier concentration of 6.38 × 10^{20} cm^{-3}, the γ_{us} decreases from 137.08 to 132.94 eV/Å^2, which is 3.02 % decreased. γ_{isf} also slightly decreases from 27.36 to 26.60 eV/Å^2. For the carrier concentration of 12.76 × 10^{20} cm^{-3}, the γ_{us} decreases from 137.08 to 127.61 eV/Å^2, which is 6.91 % decreased. γ_{isf} also slightly decreases from 27.36 to 25.70 eV/Å^2. The calculated shear stress required to create stacking fault for carrier concentration of 0 cm^{-3}, 6.38 × 10^{20} cm^{-3} and 12.76 × 10^{20} cm^{-3} are 15.85, 15.37, and 14.76 GPa, respectively

In the case of positive charging, for the carrier concentration of 6.38 × 10^{20} cm^{-3}, the γ_{us} decreases from 137.08 to 133.38 eV/Å^2, which is 2.70 % decreased. γ_{isf} also slightly decreases from 27.36 to 23.08 eV/Å^2. For the carrier concentration of 12.76 × 10^{20} cm^{-3}, the γ_{us} decreases from 137.08 to 130.11 eV/Å^2, which is 5.08 % decreased. γ_{isf} also slightly decreases from 27.36 to 20.32 eV/Å^2. The calculated shear stress required to create stacking fault for carrier concentration of 0 cm^{-3}, 6.38 × 10^{20} cm^{-3} and 12.76 × 10^{20} cm^{-3} are 15.85, 15.44, and 15.05 GPa, respectively.

Fig. 3.5 (a) shows the atomic structures after optimization of perfect, unstable stacking fault (γ_{us}), and intrinsic stacking fault (γ_{sf}) during symmetric prismatic slip along $\frac{1}{3}<0\bar{1}10>$. Fig. 3.5 (b) represents the evolution of the system energy difference relative to the initial state during symmetric prismatic slip upon charging.

For the symmetric prismatic slip, the slip lane slices the bond between two O layers. In the case of negative charging, for the carrier concentration of 6.38 × 10^{20} cm^{-3}, the γ_{us} decreases from 134.15 to 129.84 eV/Å^2, which is 3.21 % decreased. γ_{isf} also slightly decreases from 26.96 to 26.20 eV/Å^2. For the carrier concentration of 12.76 × 10^{20} cm^{-3}, the γ_{us} decreases from 134.15 to 124.82 eV/Å^2, which is 6.95 % decreased. γ_{isf} also slightly decreases from 26.96 to 25.33 eV/Å^2. The calculated shear stress required to create stacking fault for carrier concentration of 0 cm^{-3}, 6.38 × 10^{20} cm^{-3} and 12.76 × 10^{20} cm^{-3} are 15.51, 15.02, and 14.44 GPa, respectively.

In the case of positive charging, for the carrier concentration of 6.38×10^{20} cm^{-3}, the γ_{us} decreases from 134.15 to 129.82 eV/Å^2, which is 3.22 % decreased. γ_{isf} also slightly decreases from 26.96 to 22.89 eV/Å^2. For the carrier concentration of 12.76×10^{20} cm^{-3}, the γ_{us} decreases from 134.15 to 125.94 eV/Å^2, which is 6.12 % decreased. γ_{isf} also slightly decreases from 26.96 to 20.29 eV/Å^2. The calculated shear stress required to create stacking fault for carrier concentration of 0 cm^{-3}, 6.38×10^{20} cm^{-3} and 12.76×10^{20} cm^{-3} are 15.51, 15.01, and 14.57 GPa, respectively.

As shown in Fig 3.4 (b) and Fig. 3.5 (b), the excess charge effects on GSF energies is very weak in prismatic slip in both asymmetric and symmetric paths, compared to basal or pyramidal cases.

To obtain physical insights in to charging effects on the GSF energy of Al_2O_3, we also performed excess charge analysis by using an isosurface plot of the electron density differences $\Delta\rho^q$ for carrier concentration of $\pm 12.76 \times 10^{20}$ cm^{-3} in the transition states of basal and pyramidal slip systems. Fig. 3. 6 shows the excess charge distribution. Here, the electron depletion accumulation(depletion) region is represented yellow (blue) color. When the basal slip occurs in excess negative charging condition, the electron accumulate mostly near the Al atoms at the shear front [see Fig3. 6 (a)]. The abrupt decrease in GSF energy when negatively charged is due to Al interatomic bond formation by this excess negative charge at the shear front. The electron depletion occurs mainly near the O atoms at the shear front when the basal slip occurs in excess positive charging condition [see Fig3. 6 (b)]. When the pyramidal slip occurs in excess negative charging condition, the electron depletion occurs mainly near the Al atoms under or upper the shear front [see Fig. 3. 6(c)]. When the pyramidal slip occurs in excess positive charging condition, the electron depletion occurs mainly near the O atoms at the shear front [see Fig. 3. 6(d)].

To understand in detail, the electronic structures of the charged Al_2O_3 slip system, we calculated the atom-projected electronic densities of stats (PDOSs). In the PDOS calculation, a 7×7 uniform grid in the surface Brillouin zone (SBZ) is used in **k**-space integration. Fig. 3. 7 shows the PDOSs of the perfect and γ_{us} structure of basal slip with respect to carrier concentrations. When the strain occurs to γ_{us}, a defect state is formed as shown in Fig. 3. 6(f) in the region near 5eV. When excess electrons are injected to the system, this defect state is gradually filled with electrons as shown in Fig. 3.6(g) and (h). In the case of positive charging, the electrons are mostly ejected from O state as shown in Fig. 3. 6(i) and (j).

Fig. 3. 8 shows the PDOSs of the perfect and γ_{us} structure of pyramidal slip with respect to carrier concentrations. When the strain occurs to γ_{us}, a defect state is formed as shown in Fig. 3. 7(f) in the region under 5eV. When excess electrons are injected to the system, this defect state is gradually filled with electrons as shown in Fig. 3.7(g) and (h). In the case of positive charging, the electrons are mostly ejected from O state as shown in Fig. 3. 7(i) and (j).

3.4. Conclusion

Using DFT simulations, we studied the effects of charging on the mechanical behaviors of Al_2O_3 along the three basic slip system: basal, pyramidal and prismatic. We determined the activation barrier, the stacking fault energy, and the shear stress required to create the stacking fault upon charging. In all three slip systems, the activation barrier, the stacking fault energy, and the required shear stress are decreased. For basal slip, the negative charging decreases more GSF energies than positive charging. For pyramidal slip, the positive charging decreases more GSF energies than negative charging. For two types of prismatic slip, the charging effects is weaker than that of basal and pyramidal slips.

Our theoretical prediction may be validated that one possible physical origin of the e-beam assisted kinetic and super-plasticity of oxide materials.

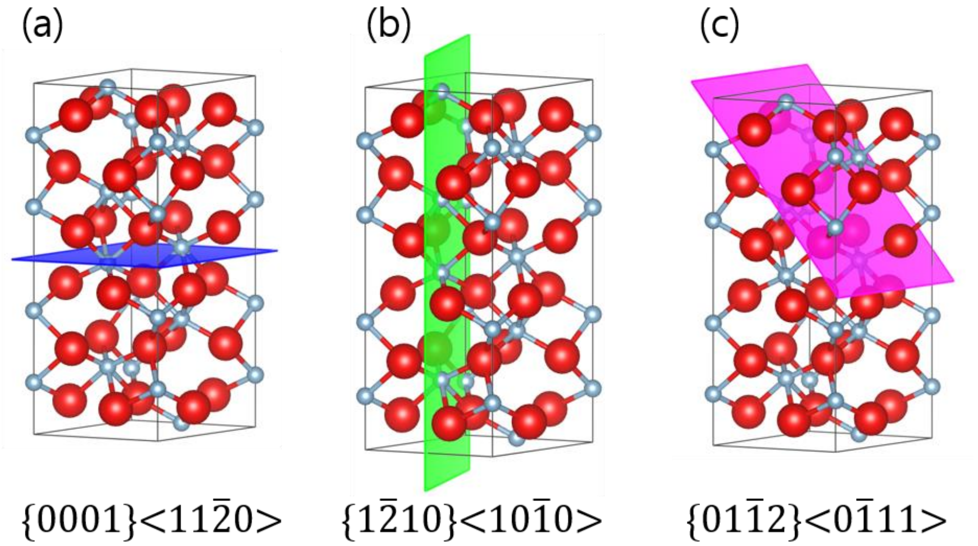

$\{0001\}\langle 11\bar{2}0\rangle$ $\{1\bar{2}10\}\langle 10\bar{1}0\rangle$ $\{01\bar{1}2\}\langle 0\bar{1}11\rangle$

Figure 3.1 Three slip systems of hcp $\alpha-Al_2O_3$: (a) A basal slip, (b) a prismatic slip, and (c) pyramidal slip. The bigger red circles represent O atoms and the smaller gray circles represent Al atoms. The blue, green, and pink plane represents the glide plane of basal, prismatic, and pyramidal slip, respectively.

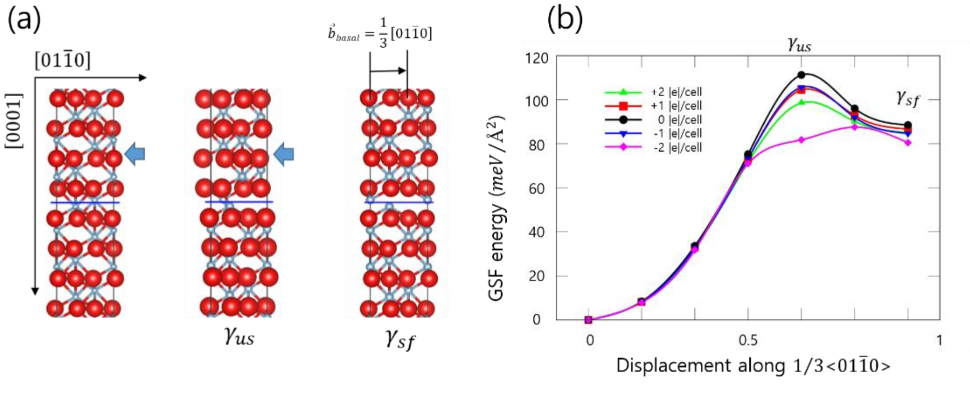

Figure 3.2 Basal slip: (a) The optimized atomic structures of perfect, unstable stacking fault (γ_{us}), and intrinsic stacking fault (γ_{sf}) during basal slip: (red particles) oxygen, (grey particles) aluminum, (blue line) shear front. (b) Evolution of the system energy during slip along the basal plane with respect to charging.

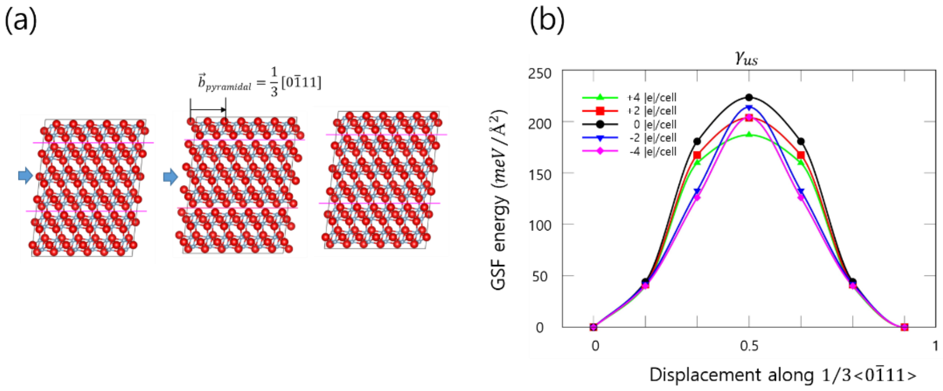

Figure 3.3 Pyramidal slip: (a) The optimized atomic structures of perfect, and unstable stacking fault (γ_{us}) during pyramidal slip: (red particles) oxygen, (grey particles) aluminum, (blue line) shear front. (b) Evolution of the system energy during slip along the pyramidal plane with respect to charging.

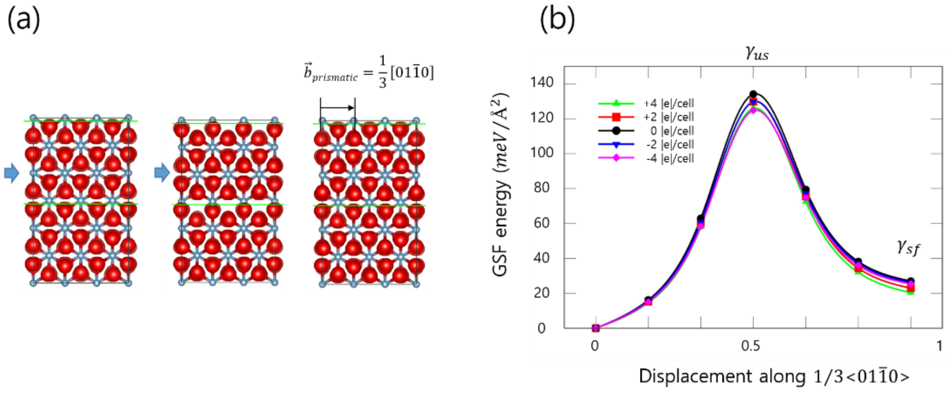

Figure 3.4 Asymmetric prismatic slip: (a) The optimized atomic structures of perfect, unstable stacking fault (γ_{us}), and intrinsic stacking fault (γ_{sf}) during asymmetric prismatic slip: (red particles) oxygen, (grey particles) aluminum, (blue line) shear front. (b) Evolution of the system energy during slip along the asymmetric prismatic plane with respect to charging.

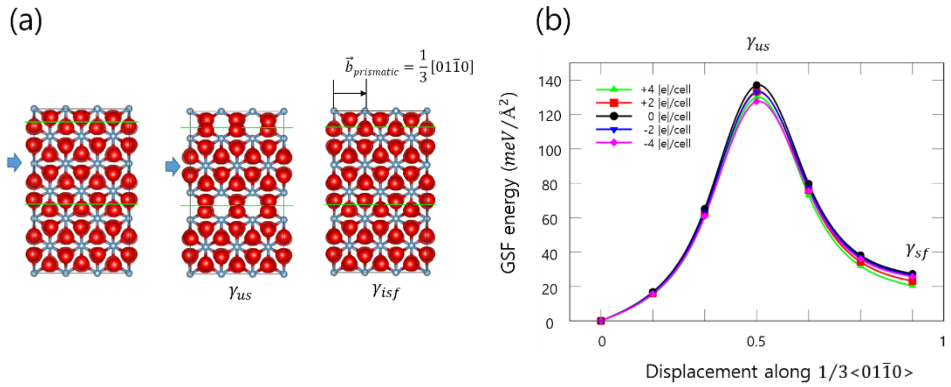

Figure 3.5 Symmetric prismatic slip: (a) The optimized atomic structures of perfect, unstable stacking fault (γ_{us}), and intrinsic stacking fault (γ_{sf}) during symmetric prismatic slip: (red particles) oxygen, (grey particles) aluminum, (blue line) shear front. (b) Evolution of the system energy during slip along the symmetric prismatic plane with respect to charging.

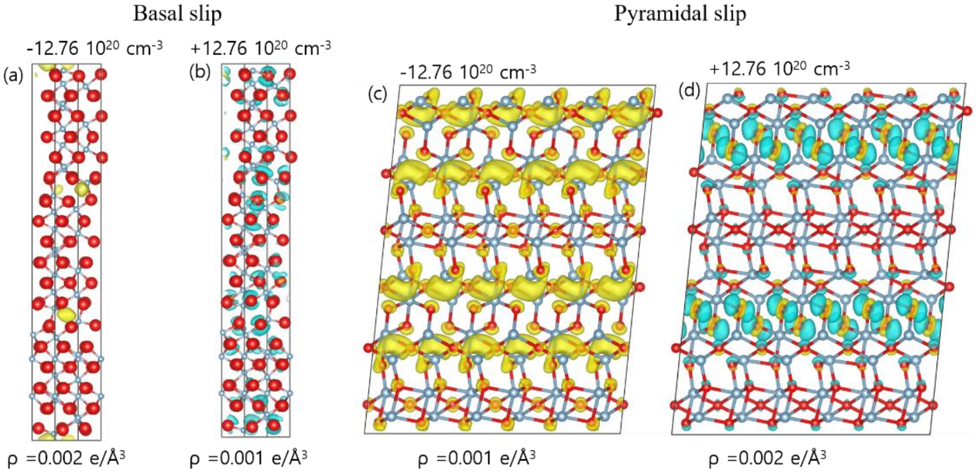
Basal slip
Pyramidal slip
-12.76 10^{20} cm^{-3}
+12.76 10^{20} cm^{-3}
(a)
(b)
-12.76 10^{20} cm^{-3}
+12.76 10^{20} cm^{-3}
(c)
(d)
ρ =0.002 e/Å^3
ρ =0.001 e/Å^3
ρ =0.001 e/Å^3
ρ =0.002 e/Å^3

Figure 3.6 Isosurface plots of electron density differences $\Delta\rho^q$ of the geometrically optimized structures of transition states of basal and pyramidal slip system with respect to carrier concentrations. Electron accumulation and depletion regions are denoted in yellow and blue, respectively.

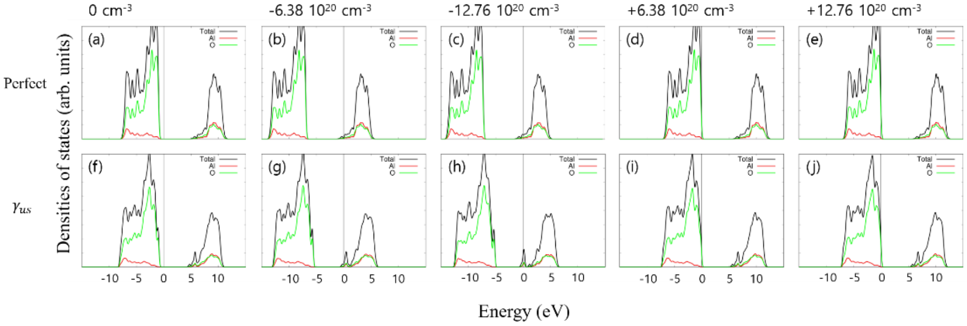

Figure 3.7 TDOSs (black line) and PDOSs of the Al (red lines) and O atoms (green lines) in the perfect [(a), (b), (c), (d), and (e)] and transition state [(f), (g), (h), (i), and (j)] structures of basal slip with respect to carrier concentrations. The energy zero is set to the Fermi energy E_F.

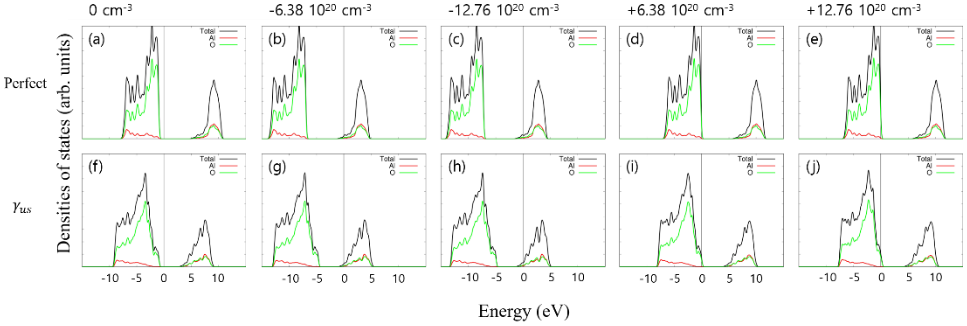

Figure 3.8 TDOSs (black line) and PDOSs of the Al (red lines) and O atoms (green lines) in the perfect [(a), (b), (c), (d), and (e)] and transition state [(f), (g), (h), (i), and (j)] structures of pyramidal slip with respect to carrier concentrations. The energy zero is set to the Fermi energy E_F.

Chapter 4. Charging effects on diffusion property of Au cluster on MgO(100)

4.1. Introduction

Metal nano clusters and thin films deposited on oxide supports are attracting increasing interest due to their broad technological applications, such as heterogeneous catalysis, gas sensors, corrosion-protective coatings, medical implants, photovoltaic devices, and microelectronic devices [25-46]. In particular, nanosized Au clusters supported on oxides have shown very active catalytic behavior for a chemical reaction like CO oxidation in contrast to Au in bulk, which is chemically inert and catalytically poorly active. Understanding the adsorption, diffusion, and electronic characteristics of Au adatoms or clusters on oxide surfaces is essential for the optimization of a catalytic process for the desired chemical reaction and product. Especially, the charge states of Au species play a critical role in the catalytic, chemical, and physical properties of the Au species on oxide supports [26-28,47-50]. For Au_7 deposited on oxidized (alkaline) TiO_2 surfaces, the cluster became cationic and exhibited high catalytic activity for the conversion of CO to CO_2 [51]. In the gas phase, anionic gold dimers,

Au_2, efficiently catalyzed the oxidation reaction of CO [52,53]. When Au_8 was bound to F_s centers (surface O vacancies) on defect-rich MgO surfaces, the cluster was easily charged due to the F_s centers with delocalized electrons. Thereby the Au_8 cluster on defective MgO was shown to be more efficient in the catalytic oxidation of CO, as compared to gold clusters on defect-poor MgO surfaces [54,55].

As another process for the charged Au species, metal-supported ultrathin oxide films could be used. For Au adatoms adsorbed on Mo-supported ultrathin MgO films, the negative charging of the Au adatoms was reported in previous theoretical works [56]. Such a behavior was explained with the electron transfer from the Mo support with low work function to the Au adatom with high electron affinity.

Indeed, scanning tunneling microscopy measurements showed images of the ordered arrays of Au adatoms on MgO/Ag(100) surfaces[57]. It was explained by charge transfer from the substrate to the Au adatoms.

Despite these studies, to our knowledge, an understanding of the adsorption properties of charged Au adatoms on oxide supports remains uncertain, in contrast to numerous studies of charged metal clusters in the gas phase. Charge state is also important in various material processes[1]. When two identical specimens were put on the ground substrate and the floating substrate and experimented under the same conditions, the two specimens showed completely different microstructure in CVD, plasma enhanced dewetting and recrystallization [5,74,75].

As a prototype of the ionic−oxide support, a MgO(100) surface has been most widely considered due to its favorable physical properties, such as its simple atomic structure, strong ionic bonding characteristics, and good chemical stability [76−78].

In this work, the adsorption and the diffusion of the charged Au adatoms on MgO(100) surfaces were studied by carrying out *ab−initio* total−energy and electronic−structure calculations based on the density functional theory (DFT)[79,80]. For the Au adatoms, adsorption structures, energetics, diffusion, and their associated electronic properties were investigated.

The calculations showed significant roles of the charge states of Au on MgO(100) in their structural, physical, chemical, and dynamic properties, which are key factors in understanding metal adatoms on oxide supports.

4.2. Compitational Details

All the total–energy and electronic–structure calculations were performed using the spin–dependent DFT as implemented in the code of the Vienna Ab–initio Simulation Package (VASP) [59,60]. For the exchange–correlation functional, the generalized–gradient approximation (GGA) of Perdew–Burke–Ernzerhof (PBE) expression was used [61]. The electron–ion interactions were treated with the projector augmented–wave (PAW) method [62]. The electronic wave functions were expanded by a plane wave basis set with an energy cutoff of 400 eV.

To simulate the adsorption and the electronic structures of Au adatoms on MgO(100), we used a repeating slab structure consisting of four MgO layers with a 15 Å vacuum region along the surface normal direction and a 3×3 surface unit cell (see Fig. 4.1). The Au adatom was adsorbed only on the upper side of the slab. For the MgO slab, the theoretical GGA–PBE equilibrium lattice constant ($\mathbf{a}_0$ = 4.24Å) of bulk MgO, which agrees well with the experimental data ($\mathbf{a}_{0,\ \mathrm{expt}}$= 4.21Å)[81] was used. The **k**–space integration was done with a summation over a uniform mesh of 9 **k** points in the surface Brillouin zone (SBZ) of the 3×3 surface unit cell. We relaxed all the atoms except for the Mg and the O atoms in the bottom two MgO layers fixed at their bulk positions. Geometry optimization was performed until the remaining forces of the atoms were smaller than 0.02 eV/Å.

To calculate the surface diffusion energy barrier of the Au adatom on MgO(100), we used the climbing image nudged elastic band (CI-NEB) method [82], where seven images of intermediate configurations along the minimum energy pathway connecting the two neighboring most stable adsorption sites were used.

For more detailed analysis of the interactions of the Au adatom with the neighboring Mg and/or O atoms, projected crystal orbital Hamilton population (pCOHP) analysis, which is a partitioning scheme of the Kohn-Sham band-structure energy in the plane-wave DFT calculations in terms of orbital-pair contributions, was performed using the Local-Orbital Basis Suite Towards Electronic-Structure Reconstruction (LOBSTER) package [83-85].

The bond-analytical pCOHP provides quantitative information for bonding, nonbonding, and antibonding contributions in the plane-wave DFT calculations [86].

4.3. Result and Discussions

For the adsorption of a Au adatom on ionic MgO(100) surfaces, there are three possible adsorption sites: sites on top of a surface O anion (atop O), on top of a surface Mg cation (atop Mg), and in a surface hollow site (*H*) (see Fig. 4.1). The energetically most stable adsorption structure is determined by comparing calculated total energies at the surface adsorption sites. Before investigating the charging effects on the adsorption of Au on MgO(100), we briefly describe the previous calculation results for the adsorption and the diffusion of uncharged Au (charge-neutral Au^0) on MgO(100). It is well known that the energetically most stable adsorption site is located at the atop O site and that the Au^0 adatom diffuses on MgO(100) by hopping over the *H* site [76-78].

In the present calculations, the atop O site shows a lower energy than the other adsorption sites in agreement with the previous studies [76-78] and the Au-O distance of 2.25 Å shorter than the corresponding values at the atop Mg and the *H* sites is obtained (see Table 4.1). The surface diffusion energy barrier obtained by using the CI-NEB method is 0.25 eV and the transition state for the surface diffusion is found to be located at the *H* site.

Next we investigate the charging effects on the adsorption properties of Au on MgO(100) by carrying out total−energy calculations of charged Au on MgO(100). Table 4.1 shows the structural properties and the energetics for the adsorption of charge−neutral and charged Au adatoms on MgO(100). In the case of the positively charged Au (Au^{+}), the atop O site is found to be favored over the other adsorption sites, in agreement with the case of Au^{0}, and the total energy at the atop O site is 0.30 eV lower than that at the H site. Due to the enhanced Coulomb interaction between Au^{+} and the anionic surface O atom, the Au^{+}−O bond distance is highly shortened in comparison to the charge−neutral case and indeed the bond distance value of 2.02 Å is much shorter than that of 2.25 Å for Au^{0}. The transition state for the surface diffusion is located at the *H* site as obtained for Au^{0}. The surface diffusion barrier of 0.30 eV for Au^{+} is higher than that of 0.25 eV for Au^{0}.

In the case of the negatively charged Au (Au^{-}), the most stable adsorption site is located at the atop Mg cation site, in contrast to the adsorption of Au^{0} and Au^{+}. The Au^{-}−Mg bond distance of 2.73 Å is obtained and is slightly elongated in comparison to the corresponding value of 2.69 Å for Au^{0}. The surface diffusion of the Au^{-} adatom on MgO(100) occurs by a hopping process over the *H* site and the transition state for the surface diffusion is the *H* site. The surface diffusion barrier obtained with the CI−NEB method is 0.03 eV much lower than the corresponding values for Au^0 and Au^+.

In order to obtain physical insights into the charging effects on the adsorption of Au on MgO(100), we also performed the charge analysis by using the isosurface plot of the electron density difference $\Delta\rho^q$ for each charge state q = +, −, as shown in Fig. 4.2:

$$\Delta\rho^q = \rho_{Au^q/MgO} - \rho_{Au^0/MgO}$$

$\rho_{Au^q/MgO}$ is the electron density of Au^q/MgO(100) and $\rho_{Au^0/MgO}$ is the electron density of the frozen Au^0/MgO(100) surface with Au^0 instead of Au^q. For Au^+ (Au^-) at all the adsorption sites on MgO(100), the electron depletion (accumulation) occurs mostly near the Au adatom and partially at the surface O atoms near the Au adatom, as shown in the upper (lower) panel of Fig. 4.2. A Bader charge analysis [87−89] was also carried out to obtain quantitative information on the charge rearrangement for the charged Au adatom on MgO(100). The obtained results are presented in Fig. 4.3. In the case of the most stable adsorption of Au^+ at the atop O site, the Bader charges q_{Au} and q_{O} are +0.29 |e| and −1.26 |e|, respectively. The values of the Au and the O atoms are +0.57|e| and +0.17 |e| larger than the corresponding values of −0.28|e| and −1.43|e| for Au^0 at the atop O site of MgO(100), respectively. In the case of the most stable adsorption of Au^- at the atop Mg site, q_{Au} and q_{Mg} are −0.87|e| and +1.64|e|, respectively. The value of the Au atom is −0.65|e| lower than q_{Au} of $-0.22|e|$ for Au^0 at the atop Mg site of MgO(100).

To understand in detail the electronic structures of the charged Au atom on MgO(100), we calculated the atom-projected spin-polarized electronic densities of states (PDOSs). In the PDOS calculations, 49 **k**-points in the SBZ were used. Figure 4.4 shows the PDOSs for the charge-neutral and charged Au adatoms on MgO(100). For Au^0 on MgO(100), the Au 5*d*-derived states are formed below the top of the MgO valence band, while the Au 6*s*-derived states are formed in the band gap region of MgO. The Au 6*s*-derived states are half-filled and spin-polarized.

When Au is charged, the electronic structures are significantly affected. For Au^+ on MgO(100), the Au 5*d*-derived states move towards the lower energy with respect to the MgO valence band and the Au 6*s*-derived states are formed near the top of the MgO valence band. The Au 6*s*-derived states are fully empty and spin-unpolarized. As a result, the Fermi energy E_{F} is located at the top of the MgO valence band.

For Au^- on MgO(100), the Au 5*d*- and 6*s*-derived states are formed in the lower and the middle band gap region, respectively. The upper Au 6*s*-derived states are fully occupied and are spin-unpolarized. This feature leads to the location of E_{F} at a higher energy with respect to the top of the MgO valence band than that for Au^0 on

MgO(100). It is also noted that the energy differences between the PDOS peaks of the 6*s*- and the 5*d*-derived states are strongly associated with the charge states of Au for all the adsorption sites. The energy differences are found to increase in the order $Au^+ > Au^0 > Au^-$.

For a microscopic understanding of the atomic bonds between the charged Au and the MgO surface atoms, we calculated the pCOHP. In Fig. 4.5, the −pCOHPs, where the positive (negative) values denote bonding (antibonding), are presented for Au−O and/or Au−Mg bonds in the adsorption of the charge-neutral and charged Au adatoms on MgO(100). For the most stable adsorption of Au^+ at the atop O site, the spin-up and -down Au−O antibonding peaks are seen at an energy of +0.20 eV above E_F. This is in contrast to the result for the most stable adsorption of Au^0 at the atop O site of MgO(100), where the −pCOHP peaks of the filled spin-up and empty spin-down antibonding states are seen near E_F. This explains well the enhanced bonding of Au^+ to the surface O atom of MgO by emptying the spin-up antibonding states, as compared to the adsorption of Au^0 at the atop O site of MgO(100).

For the most stable adsorption of Au^- at the atop Mg site,

the −pCOHP peaks of the filled spin-up and -down Au−Mg bonding states are seen at an energy of −0.45 eV below E_F, in contrast to the filled spin-up and empty spin-down Au-Mg bonding states for Au^0 at the atop Mg site. When Au^- adsorbs at the atop O site, the -pCOHP shows almost non-bonding characteristic, as compared to the adsorption of Au^0 at the atop O site. This supports the favorable adsorption of Au^- at the atop Mg site rather than at the atop O site.

4.4. Conclusion

By employing the DFT calculations, we investigated the charging effects on the adsorption and the diffusion properties of Au adatoms on MgO(100) surfaces. The optimized structures and energies of the charge-neutral and charged Au adatoms on MgO(100) were calculated.

For Au^+, the most stable adsorption site was the atop O site, coincident with the case of the charge-neutral Au^0. The Au^+-O bond distance was highly shortened in comparison to the Au^0 case, which indicates the enhanced adsorption of Au^+ at the atop O site of MgO(100) as compared to the Au^0 case. The surface diffusion barrier by a hopping process over the H site was 0.30 eV, larger than that (0.25 eV) for Au^0.

For Au^-, the most stable adsorption site was the atop Mg site, in contrast to the atop O site obtained for Au^0 and Au^+. The surface diffusion occurred by a hopping process over the *H* site and the surface diffusion barrier was very low (0.03 eV), in comparison to those for Au^0 and Au^+.

The charge analysis showed that the electron depletion (accumulation) occurred mostly near the Au^+ (Au^-) adatom with a partial rearrangement at its nearby surface O atoms. Further analysis of the electronic structures exhibited the significant changes in the positions of the Au 5*d*- and 6*s*- derived peaks and the Fermi energy E_F with respect to the top of the MgO valence band, which are very important in determining the chemical or physical activities of oxide-supported metal systems.

The pCOHPs were also calculated for the atomic bonds between the charged Au and the MgO surface atoms. The pCOHP results well explained the adsorption behavior of Au^+ and Au^- different from that of Au^0.

These results are expected to provide fundamental and very important information to identify the charge state of Au adatoms adsorbed on MgO(100). Furthermore, the results can also provide physical and chemical insights into an understanding of the microscopic mechanism underlying the growth of thin films from charged species, which has exhibited growth behaviors different from conventional film growth processes with charge-neutral species.

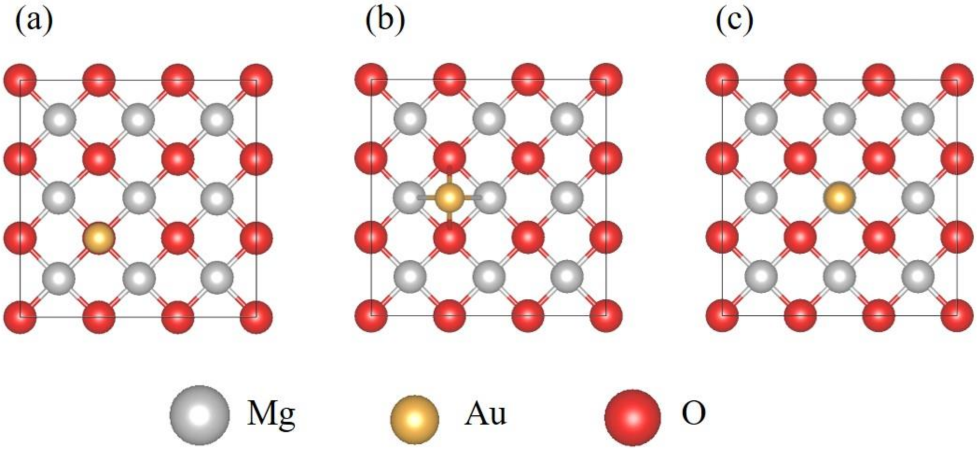

Figure 4.1 Top views of the adsorption structures of Au adatoms on MgO(100) surfaces: adsorption (a) on top of a surface O site, (b) in a surface hollow site (*H*), and (c) on top of a surface Mg site. The $p(3\times3)$ surface unit cell used in the calculations is denoted by black lines.

Table 4.1 Calculation results for the physical properties of the charge-neutral and charged Au adatoms at the three adsorption sites on MgO(100): interatomic distance *d* of Au with the neighboring atoms and energy ΔE relative to that of the most stable adsorption site.

	O top		**Hollow**		**Mg top**	
	d_{Au-O} [Å]	ΔE [eV]	d_{Au-O} (d_{Au-Mg}) [Å]	ΔE [eV]	d_{Au-Mg} [Å]	ΔE [eV]
Au^0	2.25	0.00	2.80 (2.82)	**0.25**	2.69	0.47
Au^+	2.02	0.00	2.36 (2.68)	**0.30**	2.55	1.04
Au^-	2.91	0.19	3.20 (2.97)	**0.03**	2.73	0.00

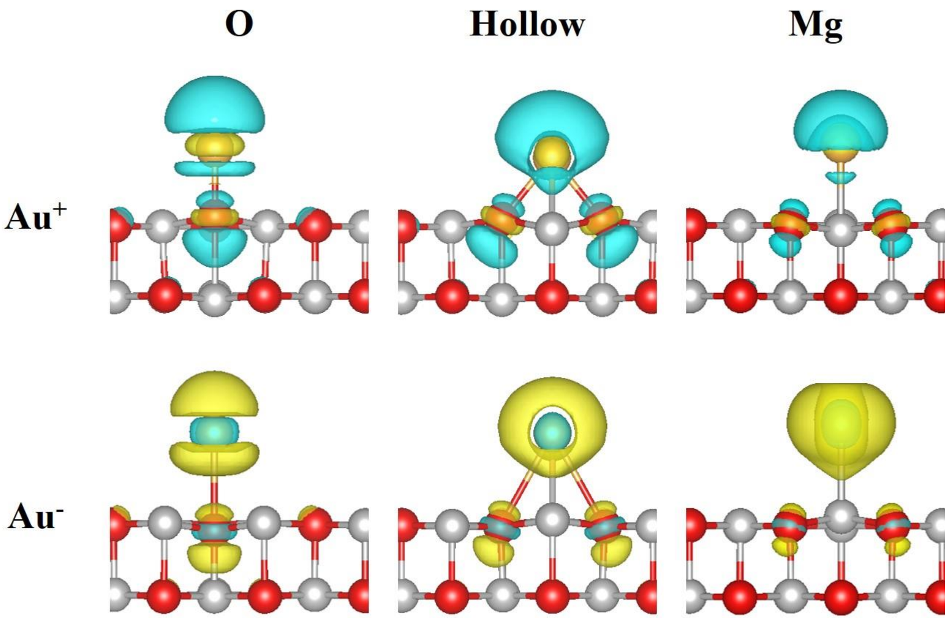

Figure 4.2 Isosurface plots of electron density differences $\Delta\rho^q$ superimposed on side views of the geometrically optimized structures if the charged Au adatoms at the three adsorption sites on MgO(100). Electron accumulation and depletion regions are denoted in yellow and blue, respectively. The isosurface levels are ±0:003 electrons/bohr^3.

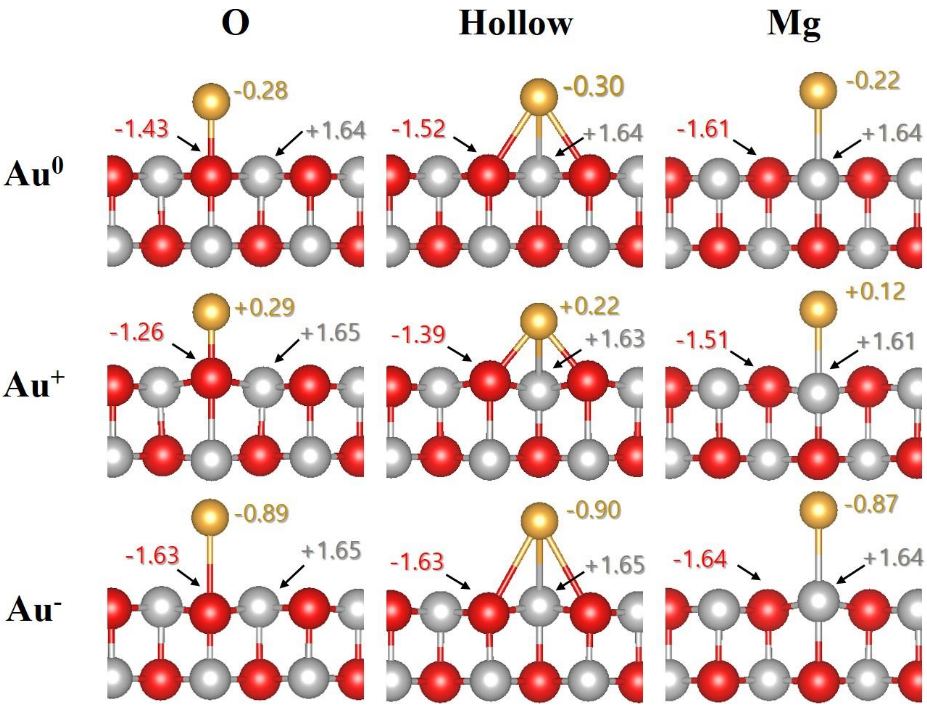
O
Hollow
Mg
Au⁰
Au⁺
Au⁻
-0.28
-1.43
+1.64
-0.30
-1.52
+1.64
-0.22
-1.61
+1.64
+0.29
-1.26
+1.65
+0.22
-1.39
+1.63
+0.12
-1.51
+1.61
-0.89
-1.63
+1.65
-0.90
-1.63
+1.65
-0.87
-1.64
+1.64

Figure 4.3 Side views of the geometrically optimized atomic structures of the charge−neutral and charged Au adatoms at the three adsorption sites on MgO(100). The numbers represent Bader charges (in units of $|e|$) of Au and its neighboring surface atoms.

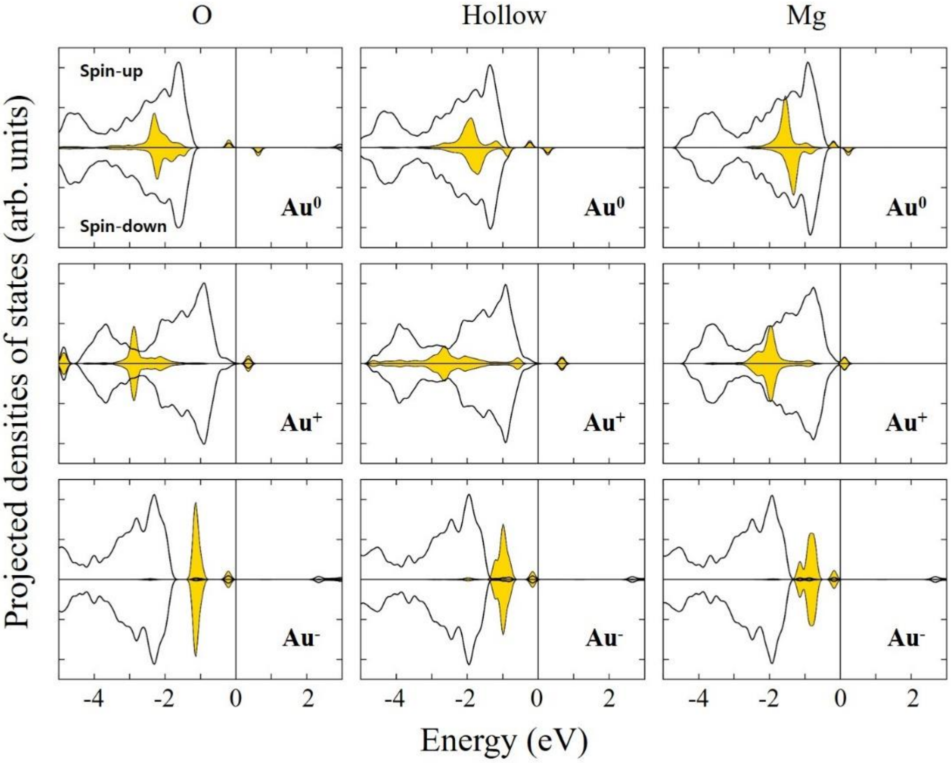

Figure 4.4 PDOSs of the Au (shaded) and MgO atoms (black lines) in the top two MgO layers for the charge−neutral and charged Au adatoms at the three adsorption sites on MgO(100). The energy zero is set to the Fermi energy E_F. It is herein noted that the PDOS peaks in the band gap region of MgO consist of hybrid states of Au and the surface atoms of MgO(100).

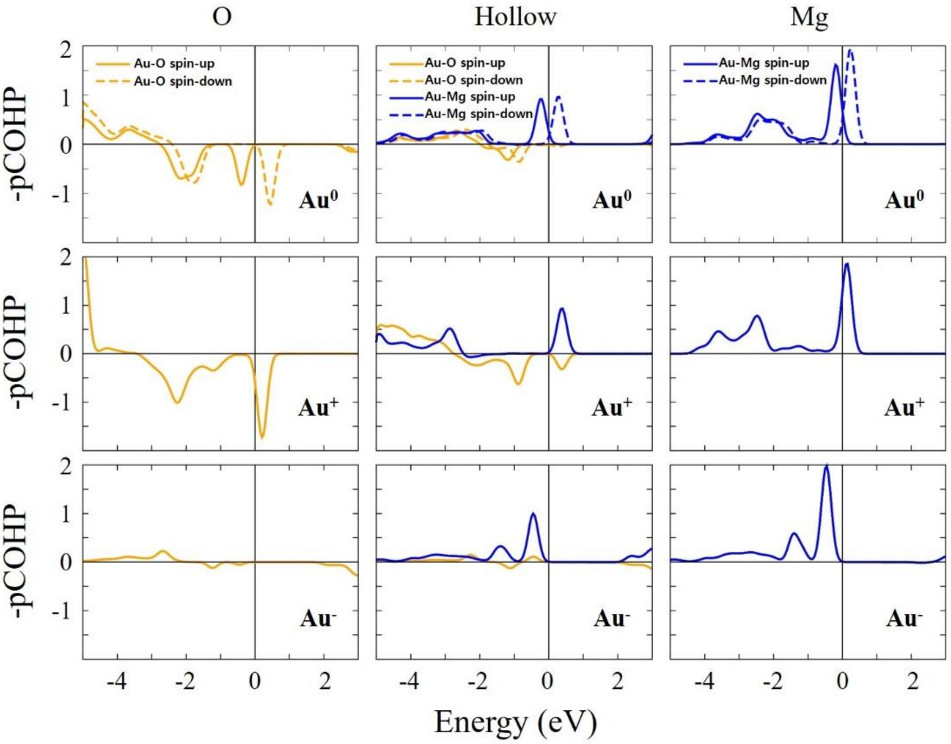

Figure 4.5 Projected crystal orbital Hamilton population analysis of atomic bonds during the adsorption of charge−neutral and charged Au adatoms at the three adsorption sites on MgO(100) surfaces. The energy zero is set to the Fermi energy E_F.

Chapter 5. Charging effects on diffusion property of Au cluster on MgO(100)

5.1. Introduction

Growth of oxide-supported metal particles and thin films has attracted widespread interest in fields, such as heterogeneous catalysis, gas sensors, corrosion protective coatings, and microelectronic devices [25-29,31-46,90]. In particular, among metal particles, Au nanoclusters supported on oxides are of special interest because of their exceptional catalytic properties [26-28,47-50]. Catalytic reactivities of Au nanoclusters depend critically on their charge state and atomic structure. In the previous studies [52-55], charged Au nanoclusters promoted catalytic reactions more efficiently than charge-neutral Au nanoclusters both in the gas phase and the oxide-supported system.

In the gas phase, a negatively charged gold dimer (Au_2^-) is more efficient than a neutral gold dimer (Au_2^0) in the oxidation reaction of CO [52,53]. On defect-rich MgO(100) surfaces with surface oxygen vacancies (F_s centers), a Au_8 cluster on F_s with delocalized electrons was negatively charged and promoted the oxidation reaction of CO.

For Au nanocluster deposited on metal-supported ultrathin oxide films, it could be charged by electron tunneling from metal supports with low work function to Au species with high electron affinity. When Au clusters were deposited on 3ML-MgO/Mo(100), the Au clusters were negatively charged. The charge state of Au nanoclusters could also affect the atomic structures of the Au species, which are one of key issues in determining their catalytic activities [91,92]. Scanning tunneling microscopy measurements showed that Au species on 3ML-MgO/Ag(100) had two-dimensional (2D) structures, while Au species deposited on 8ML-MgO/Ag(100) had three-diemensional (3D) structures [57,93,94]. In addition, for the growth processes of thin films and nanostructures on insulating substrates, the enhanced kinetic behavior was observed in charged species, as compared with that in charge-neutral species on conducting substrates [1]. In the in-situ transmission electron microscopy observation, small metal particles deposited on insulating oxides changed their atomic structures spontaneously in a few seconds [20]. The dewetting kinetics of Sn and Au thin films and the recrystallization of Fe-1%Si steel on insulating substrates were enhanced by employing charging processes [5,75]. Despite these studies, the atomic structures and dynamics of charged metal clusters formed on oxides remain uncertain in both theories and experiments.

As a model system to study charged metal clusters on oxides, we herein consider Au dimer, the simplest form of metal clusters adsorbed on MgO(100), of which a charge-neutral system has been extensively studied using various experimental techniques and computational methods [57,92,93,95-98].

The purpose of this study is to understand charging effects on the adsorption structure and diffusion of Au dimer on MgO(100). In order to find the most stable adsorption structure and the diffusion process of the Au dimer for each charge state, we carried out *ab-initio* total energy calculations based on the density functional theory (DFT) [79,80]. For more detailed information on the interactions between the Au dimer and the underlying surface atoms, the analysis of the electronic structures and the charge distribution were also performed.

5.2. Computational Details

All the calculations in this study were performed using the spin-polarized DFT with the plane-wave code of the Vienna Ab-initio Simulation Package(VASP) [59,60]. The generalized gradient approximation (GGA) of the Perdew-Burke-Ernzerhof (PBE) expression was used for the exchange correlation (XC) energy [61]. For the electron-ion interaction, the projector-augmented wave

(PAW) method was used [62].

We used a repeating slab geometry with a 15 Å vacuum thickness along the surface normal direction. The slab structure consisted of three MgO layers. The Au dimer was adsorbed only on the upper side of the slab with a 4×4 surface unit cell. For the lattice constant of MgO, the calculated GGA−PBE value (a_0 = 4.24Å) in bulk MgO was used. Plane waves with an energy cutoff of 400 eV were used to describe the electronic wave functions. The **k**−space integration was performed using a 3×3 uniform grid in the surface Brillouin zone (SBZ) of the surface unit cell. The bottommost MgO layer was fixed at its bulk position, whereas all the other atoms were fully relaxed. The geometry was optimized until the remaining atomic forces were smaller than 0.02 eV/Å.

To calculate the surface diffusion barrier of the Au dimer on MgO(100), the climbing image nudged elastic band (CI−NEB) method [82] was used with nine images of intermediate configurations between the two neighboring most stable adsorption sites.

5.3. Results and Discussions

For the dimer adsorption on MgO(100), two different configurations were considered: the upright (*S*) and flat-lying (*P*) dimers. For each configuration, there are three possible surface adsorption sites: sites on top of a surface O anion, on top of a surface Mg cation, and in a surface hollow (*H*) site.

Figure 5.1 shows representative adsorption structures of Au dimers on MgO(100). Table 5.1 represents the calculation results of the dimer adsorption at the three stable adsorption structures in neutral, positive, and negative charge states. The relative energies (ΔE) denote the total energies relative to that of the most stable adsorption structure in each charge state.

In the case of a charge-neutral Au dimer (Au_2^0), the most favored adsorption structure is the S_O dimer configuration in Fig. 5.1 (a) as presented in the previous study. The S_H and P_{O-H-O} structures in Figs. 5.1 (b) and (c) have ΔE of 0.69 and 0.96 eV, respectively, with respect to the most stable S_O configuration. The upright S_O and S_H dimers have dimer bond distances d_{Au-Au} similar to that of the gas-phase dimer (2.50 Å), while the flat-lying P_{O-H-O} dimer has d_{Au-Au} elongated to 2.57 Å. The magnetic moments of Au_2^0 are 0.00 μ_B irrespective of adsorption structures.

In the case of a positively charged Au dimer (Au_2^+), the most stable adsorption structure is the S_O configuration same as Au_2^0. The S_H and P_{O-H-O} structures in Figs. 5.1 (b) and (c) have $\varDelta E$ of 0.47 and 0.27 eV, respectively, with respect to the most stable S_O configuration.

As compared with the dimer bond distance of gas-phase Au_2^+ (2.60 Å), d_{Au-Au} values of S_O and S_H are highly shortened to 2.50 and 2.49 Å, respectively, while d_{Au-Au} of P_{O-H-O} is elongated to 2.66 Å. d_{Au-O} values of Au_2^+ are shorter than the corresponding values of Au20$ for all the three configurations, respectively. The magnetic moments of Au_2^+ depend on the adsorption structures. The values are in the range from 0.32 to 1.00 $\mu_{B.}$

In the case of a negatively charged Au dimer (Au_2^-), the most stable adsorption structure is the $P_{Mg-H-Mg}$ configuration in Fig. 5.1(d). The P_{H-O-H} and P_{H-Mg-H} structures in Fig 5.1 (e) and (f) have $\varDelta E$ of 0.06 and 0.11 eV, respectively, with respect to the most stable $P_{Mg-H-Mg}$ configuration. d_{Au-Au} values of Au_2^- for all the three configurations are very close to that (2.62 Å) in the gas phase of Au_2^-. The magnetic moments of Au_2^- are 1.00 Au_2^+ irrespective of the adsorption structures.

To calculate diffusion barriers of the charge-neutral and charged Au dimers, we carried out CI-NEB calculations. The CI-NEB calculation results are shown in Fig. 5.2 and summarized in Table 5.2.

Au_2^0 diffusion may proceed by hopping between the most stable adsorption S_O sites. The hopping diffusion of Au_2^0 occurs along the $S_O - S_H - S_O$ path. The transition state for the hopping diffusion is S_H. The barrier of 0.69 eV, in agreement with the values in previous studies, is obtained. Another possible diffusion process is a leapfrog movement, where Au_2^0 moves from the most stable configuration S_O to configuration P_{O-H-O} and again to the most stable configuration S_O at the neighboring O site. The transition state for the leapfrog diffusion is shown in Fig. 5.2 (a). The leapfrog surface diffusion barrier is 1.01 eV. This shows that Au_2^0 prefers the diffusion by a hopping process rather than by a leapfrog process.

In the case of Au_2^+, the hoping diffusion of Au_2^+ occurs along the $S_O - S_H - S_O$ path with S_H as the transition state. The hopping diffusion barrier of Au_2^+ is 0.68eV, which is very close to that of Au_2^0. The leapfrog diffusion occurs along the path from S_O to P_{O-H-O} to S_O at the neighboring O site. The P_{O-H-O} configuration is a metastable state and the transition state is shown in Fig. 5.2 (b). The leapfrog diffusion barrier is 0.42 eV, which is much lower than the hopping diffusion barrier of Au_2^+. This means that Au_2^+ prefers the diffusion by a leapfrog process rather than by a hopping process. Interestingly, the leapfrog diffusion barrier of Au_2^+ is much smaller than the barrier of the hopping diffusion preferred for Au_2^0.

In the case of Au_2^-, diffusion may occur by hopping between the most stable adsorption $P_{\mathrm{Mg-H-Mg}}$ sites. The hopping diffusion of flat-lying Au_2^- is anisotropic, so there are two possible paths. One is the dimer hopping (hopping through O) from the most stable $P_{\mathrm{Mg-H-Mg}}$ configuration to the metastable $P_{\mathrm{H-O-H}}$ configuration to the most stable $P_{\mathrm{Mg-H-Mg}}$ configuration at the neighboring sites, where the center of the dimer bond passes through a surface O atom [Figs. 5.1 (e)]. The transition state is shown in Fig. 5.2 (c).

Another is the dimer hopping (hopping through Mg) from most stable $P_{\mathrm{Mg-H-Mg}}$ to metastable $P_{\mathrm{H-Mg-H}}$ to most stable $P_{\mathrm{Mg-H-Mg}}$ at the neighboring sites, where the center of the dimer bond passes through a surface Mg atom [Figs. 5.1(f)]. The transition state is shown in Fig. 5.2 (c). The surface diffusion barrier of Au_2^- by the hopping through the surface Mg atom is 0.15 eV.

The other possible diffusion process is the walking diffusion, where Au_2^- of most stable $P_{\mathrm{Mg-H-Mg}}$ rotates 45° about one of the Au dimer atoms. The 45°-rotated configuration $P_{\mathrm{Mg-H-Mg}}(\mathrm{R45°})$ and the transition state are shown in Fig. 5.2(c). The surface diffusion barrier of Au_2^- by the walking process is 0.12 eV.

All the calculations of the surface dynamics for Au_2^+ and Au_2^- clearly suggest that *charge states of* Au *dimers significantly affect both their diffusivity and diffusion processes on* MgO(100).

To obtain more detailed physical insights into the adsorption of charge-neutral and charged Au dimers on MgO(100), we also performed the electronic structure calculations. Fig. 5.3 presents the calculated atom-projected spin-polarized electronic densities of states (PDOSs). In the PDOSs calculations, denser 49 **k**-points in the SBZ were used. In the present results, the PDOSs of Au_2^0 adsorbed on MgO(100) are spin-unpolarized, in agreement with the previous study. For the S_O, S_H, and P_{O-H-O} configurations, the Fermi energy positions ($\varDelta E_F$) relative to the valance band maximum (VBM) of MgO are +0.35, +0.45, and +0.70 eV, respectively. The Au 5*d*-derived states are formed below the VBM of MgO, while the Au 6*s*-derived states are formed near the VBM and in the gap of MgO. For the S_O, S_H, and P_{O-H-O} configurations, the PDOS peak positions ($\varDelta_{HO}$) of the highest-occupied states of Au relative to the VBM of MgO are +0.17, +0.30, and +0.52 eV, respectively, and the PDOS peak positions ($\varDelta_{LO}$) of the lowest-unoccupied states of Au relative to the VBM of MgO are +2.87, +2.37, and +1.81 eV, respectively. When the Au dimer is charged, the electronic structures are significantly affected. For Au_2^+ on MgO(100), the PDOSs are spin-polarized and the magnetic moments depend on the adsorption structures as shown in Table 5.1. The Fermi energy positions move towards a lower energy with respect to the VBM of MgO.

For the S_{O}, S_{H}, and $P_{\mathrm{O-H-O}}$ configurations, ΔE_{F} are −0.08, −0.13, and +0.36 eV, respectively. The negative values of ΔE_{F} indicate that the Fermi energy is located below the VBM of MgO.

Therefore, S_{O} and S_{H} have metallic electronic structures. Δ_{HO} of $P_{\mathrm{O-H-O}}$ is +0.17 eV. Δ_{LO} of S_{O}, S_{H}, and $P_{\mathrm{O-H-O}}$ are +2.92, +2.34 and +0.31 eV, respectively. For Au_2^- on MgO(100), the PDOSs are spin-polarized and the magnetic moments are 1.0 μ_{B} for all the three adsorption structures. The Au 5*d*- and 6*s*-derived states are formed in the lower and the middle band gap region, respectively. For the $P_{\mathrm{Mg-H-Mg}}$, $P_{\mathrm{H-O-H}}$ and $P_{\mathrm{H-Mg-H}}$ configurations, ΔE_{F} are +1.77, +1.80 and +1.78 eV, respectively. For the $P_{\mathrm{Mg-H-Mg}}$, $P_{\mathrm{H-O-H}}$, and $P_{\mathrm{H-Mg-H}}$, Δ_{HO} are +1.59,+1.64 and +1.57 eV, respectively, and Δ_{LO} are +2.19,+2.18 and +2.11 eV, respectively.

Next we examine charge distribution of the charge-neutral and charged Au dimers adsorbed on MgO(100) by calculating Bader charges. Table 5.3 summarizes the results of the Au dimer atoms and their neighboring surface atoms.

In the clean MgO(100) surface, the Bader charges of surface O and Mg atoms are −1.65 and +1.65 |e|, respectively. For all the adsorption structures of the charge-neutral and charged Au dimers, the variation in the Bader charges of their neighboring surface Mg atom is less than 0.02 |e|.

In the case of Au_2^0 on MgO(100), the surface O atom donates electrons to the Au dimer atoms, so the Bader charge of the surface O atom ranges from −1.53 to −1.44 |e| higher then that (−1.65 |e|) of the clean MgO surface. The Bader charge of the Au dimer is in the range from −0.35 to −0.30 |e|. This suggests that the Au dimer is slightly negatively charged.

When Au_2^+ is adsorbed, the Bader charge of the surface O atom ranges from −1.42 to −1.35 |e| and the Bader charge of the Au dimer is in the range from −0.04 to +0.11 |e|. The values are higher than those of Au_2^0.

The flat−lying dimer in configuration $P_{\mathrm{O-H-O}}$ is slightly positively charged, so the Au−O bond is stabilized by the Coulomb attraction, which is well reflected in the shortened Au−O bond distance as compared with that of Au_2^0. This explains why $P_{\mathrm{O-H-O}}$ is more stable than S_{H} structure for Au_2^+ unlike $Au2^0$.

For Au_2^-, the Bader charge of the surface O atom is in the range from −1.61 to −1.63 |e|, which is very close to that in the clean MgO(100) surface. The Bader charge of the Au dimer is in the range from −0.96 to −0.92 |e|. This indicates that excess electrons are located at the Au dimer.

To obtain further spatial information on the charge distribution of the charged Au dimers on MgO(100), we also performed the charge analysis by using the isosurface plot of the electron density difference $\Delta\rho^q$ for each charge state $q = +, -$, as shown in Fig. 5.4: $\Delta\rho^q = \rho_{Au_2{}^q/MgO} - \rho_{Au_2{}^0/MgO}$. Here, $\rho_{Au_2{}^q/MgO}$ is the electron density of $Au_2{}^q$ on MgO(100) and $\rho_{Au_2{}^0/MgO}$ is the electron density of frozen $Au_2{}^0$ on MgO(100) with $Au_2{}^0$ instead of $Au_2{}^q$.

For the adsorption configurations of $Au_2{}^+$ ($Au_2{}^-$) on MgO(100), the electron depletion (accumulation) occurs mostly at the Au dimer and partially at its neighboring surface O atoms. For $Au_2{}^+$, electrons are depleted mainly from the dimer region far away from the MgO surface, while for $Au_2{}^-$, electrons are accumulated at the dimer bond edges.

5.3. Conclusion

By using the DFT calculations, we investigated the effects of charging on the adsorption and diffusion of Au dimers on MgO(100) surfaces. For the $Au_2{}^+$ adsorption, the most stable adsorption structure is the upright dimer on a surface O site same as the $Au_2{}^0$ adsorption. The surface diffusion, however, proceeds by the leapfrog mechanism with the barrier height of 0.42 eV much smaller than the barrier height (0.69 eV) of the favorable hopping diffusion for $Au_2{}^0$. The smaller diffusion barrier is ascribed to the highly enhanced bonding between the positively charged Au dimer atoms and their underlying surface O atoms at the transition state for the leapfrog diffusion process that stabilizes the flat-lying dimer structures on MgO(100), as compared with Au_2^0. For the Au_2^- adsorption, the most stable adsorption structure is the flat-lying dimer on two surface Mg atoms unlike the Au_2^0 and Au_2^+ cases. The Au_2^- dimer can diffuse in various ways with the surface diffusion barrier in the range of 0.10-0.15 eV. These values are very low compared with the surface diffusion barriers for Au_2^0 and Au_2^+. The very low diffusion barriers are ascribed to the weaker bonding between the Au_2^- dimer atoms and the surface atoms as reflected in their elongated atomic distances compared with those of Au_2^0 and Au_2^+.

The enhanced surface diffusion of Au_2 on MgO(100) by both positive and negative charging is in sharp contrast with the surface diffusion behavior for a single Au adatom on MgO(100), where the surface atomic diffusion of Au is suppressed by positive charging but enhanced by negative charging [99]. The charge-enhanced kinetics for Au_2 clearly suggest that charge states of Au dimers play a crucial role in determining their diffusivity as well as the diffusion processes for on MgO(100).

For a more detailed understanding of the physical properties of the charge-neutral and charged Au dimers on MgO(100), we also performed analyses of the electronic structures, the Bader charges, and the charge distribution. These results provide very important information for understanding the charging effects on the adsorption and dynamics of the Au dimers adsorbed on MgO(100). This study is an early stage research for the new physics and chemistry of charged metal particles on insulating substrates. Further studies are needed on the effects of charging on the atomic structures and the dynamics of other metal clusters with various sizes on insulating substrates.

Furthermore, the results can also provide physical and chemical insights into an understanding of microscopic mechanisms underlying the charge-dependent kinetics such as structure instability, dewetting, and recrystallization of charged metal nanoparticles on insulators.

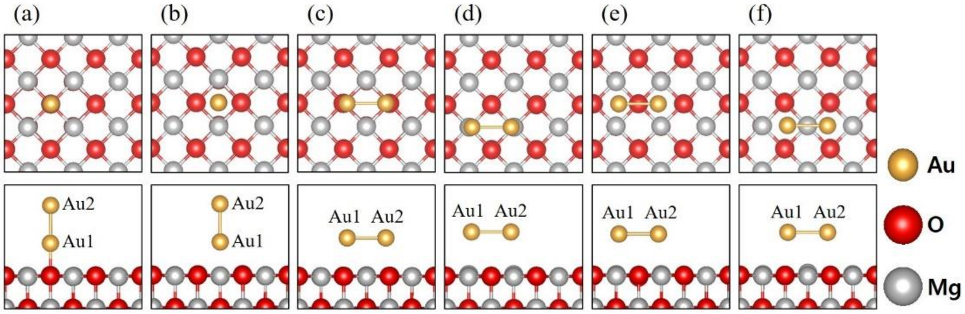

Figure 5.1 Top and side views of the adsorption structures of Au dimers on MgO(100): (a) the upright dimer on an O site (S_{O}), (b) the upright dimer on a H site (S_{H}), (c) the flat−lying dimer on two O sites ($P_{\mathrm{O\text{-}H\text{-}O}}$), (d) the flat−lying dimer on two Mg sites ($P_{\mathrm{Mg\text{-}H\text{-}Mg}}$), (e) the flat−lying dimer on two H sites with an O atom at the dimer bond center ($P_{\mathrm{H\text{-}O\text{-}H}}$), and (f) the flat−lying dimer on two H sites with a Mg atom at the dimer bond center ($P_{\mathrm{H\text{-}Mg\text{-}H}}$).

Table 5.1 Calculation results for the adsorption properties of the charge−neutral and charged Au dimers at the three stable adsorption sites on MgO(100): total energy ΔE relative to that of the most stable adsorption structure, interatomic distance d, and total magnetic moment μ.

	Structure	ΔE [eV]	$d_{\mathrm{Au\text{-}Au}}$ [Å]	$d_{\mathrm{Au\text{-}O}}$ [Å]	$d_{\mathrm{Au\text{-}Mg}}$ [Å]	μ_B
Au_2^0	Gas phase	-	2.50	-	-	0.00
	S_O	0.00	2.51	2.12	-	0.00
	S_H	0.66	2.52	2.63	2.77	0.00
	$P_{O\text{-}H\text{-}O}$	0.95	2.57	2.55	-	0.00
Au_2^+	Gas phase	-	2.60	-	-	1.12
	S_O	0.00	2.50	2.09	-	0.32
	S_H	0.52	2.49	2.43	2.71	0.74
	$P_{O\text{-}H\text{-}O}$	0.22	2.66	2.18	-	1.00
Au_2^-	Gas phase	-	2.62	-	-	1.00
	$P_{Mg\text{-}H\text{-}Mg}$	0.00	2.62	-	2.83	1.00
	$P_{H\text{-}O\text{-}H}$	0.05	2.64	3.16	3.09	1.00
	$P_{H\text{-}Mg\text{-}H}$	0.11	2.65	3.27	3.02	1.00

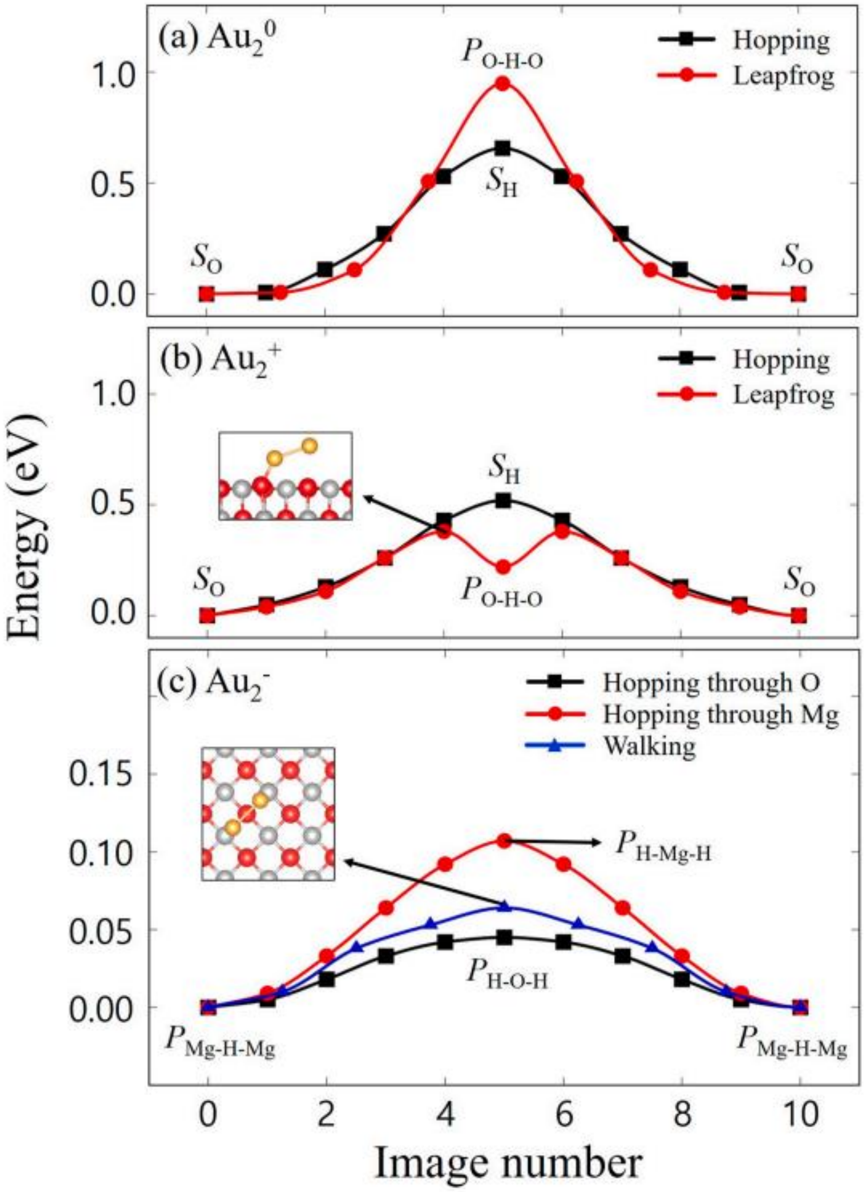

Figure 5.2 Energy profiles of the Au dimers diffusing by the indicated atomic processes on MgO(100), calculated within the CI−NEB.

Table 5.2 Calculation results for the diffusion processes and barriers of the charge−neutral and charged Au dimers (Au_2^0, Au_2^+, and Au_2^-) on MgO(100).

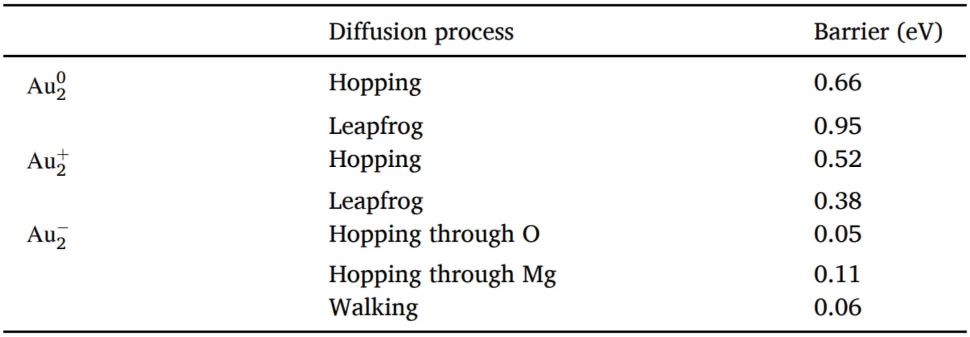

	Diffusion process	Barrier (eV)
Au_2^0	Hopping	0.66
	Leapfrog	0.95
Au_2^+	Hopping	0.52
	Leapfrog	0.38
Au_2^-	Hopping through O	0.05
	Hopping through Mg	0.11
	Walking	0.06

Table 5.3 Calculation results for the diffusion processes and barriers of the charge−neutral and charged Au dimers (Au_2^0, Au_2^+, and Au_2^-) on MgO(100).

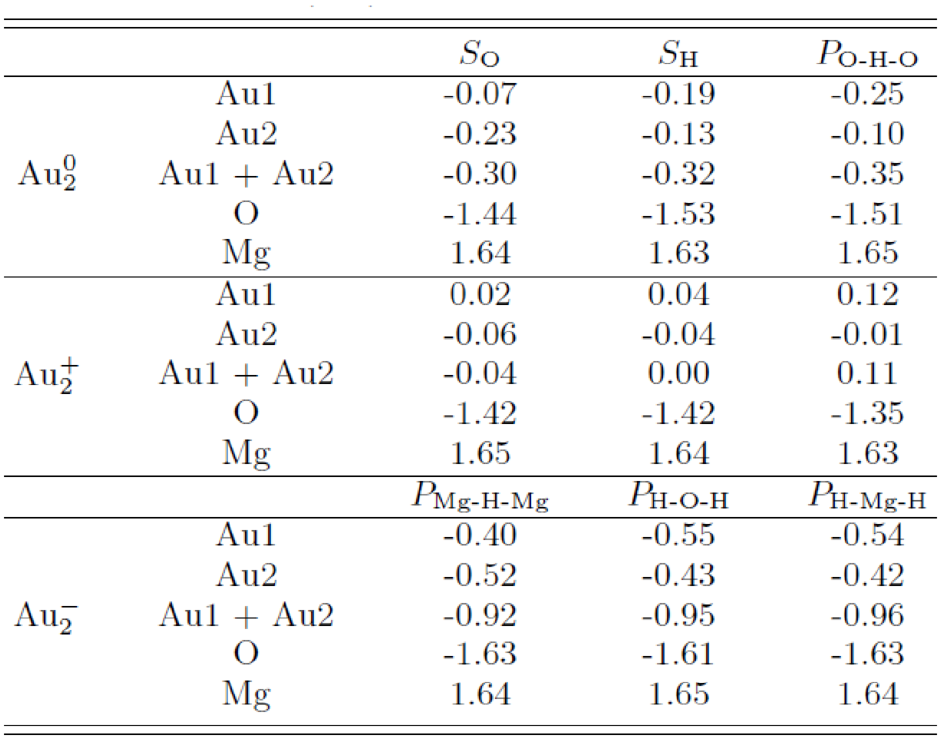

		S_{O}	S_{H}	$P_{\text{O-H-O}}$
Au_2^0	Au1	-0.07	-0.19	-0.25
	Au2	-0.23	-0.13	-0.10
	Au1 + Au2	-0.30	-0.32	-0.35
	O	-1.44	-1.53	-1.51
	Mg	1.64	1.63	1.65
Au_2^+	Au1	0.02	0.04	0.12
	Au2	-0.06	-0.04	-0.01
	Au1 + Au2	-0.04	0.00	0.11
	O	-1.42	-1.42	-1.35
	Mg	1.65	1.64	1.63
		$P_{\text{Mg-H-Mg}}$	$P_{\text{H-O-H}}$	$P_{\text{H-Mg-H}}$
Au_2^-	Au1	-0.40	-0.55	-0.54
	Au2	-0.52	-0.43	-0.42
	Au1 + Au2	-0.92	-0.95	-0.96
	O	-1.63	-1.61	-1.63
	Mg	1.64	1.65	1.64

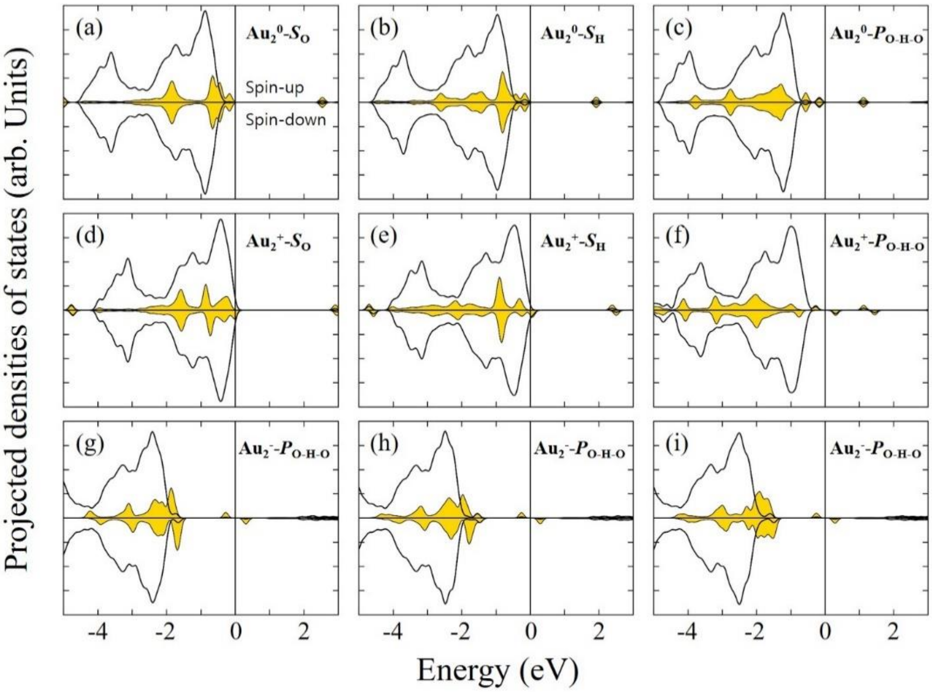

Figure 5.3 Projected spin–polarized electronic densities of states (PDOSs) of the Au dimer atoms and the MgO atoms in the top two MgO layers for the charge–neutral and charged Au dimers at the three stable adsorption sites on MgO(100). The energy zero is set to the Fermi energy E_F.

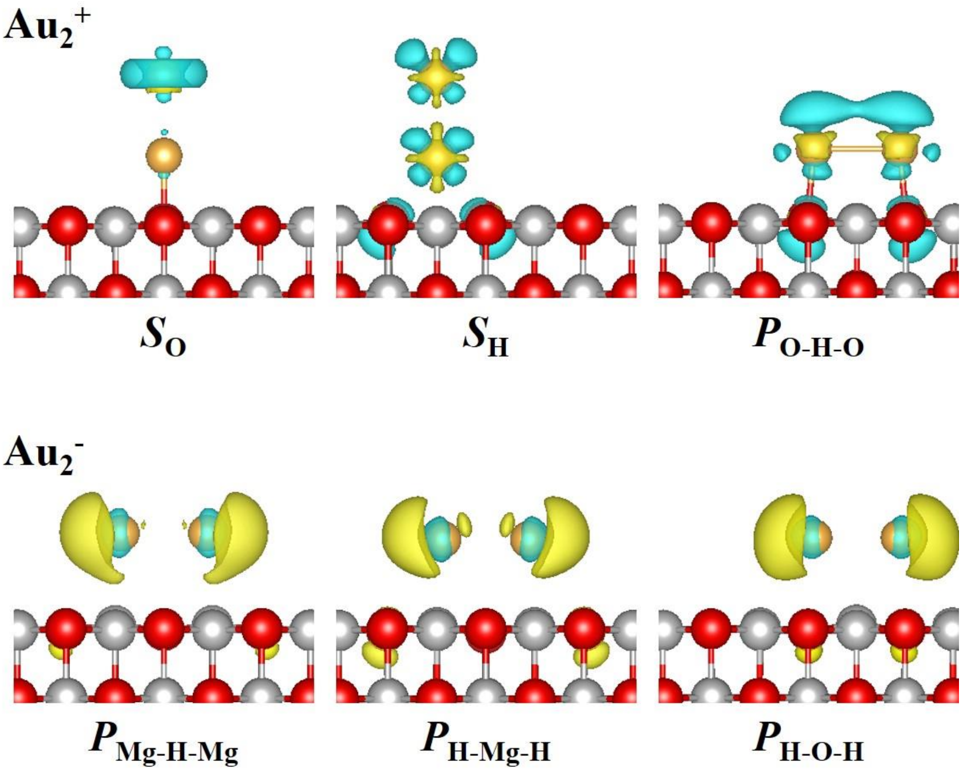

Figure 5.4 Isosurface plots of electron density differences $\Delta\rho q$ superimposed on the side views of the geometry-optimized structures of the three adsorption configurations for each charge state of the charged Au dimer on MgO(100). Electron accumulation and depletion regions are denoted by yellow and blue, respectively. The isosurface levels are ±0.002 electrons/bohr^3.

Chapter 6. Charging effects on the vibrational properties of Au and Au_2 on MgO(100)

6.1. Introduction

Metal clusters and thin films deposited on oxide supports have a great deal of interest due to their technological applications such as heterogeneous catalysis, gas sensors, corrosion–protective coatings, and microelectronic devices [25–29,31–46,90]. In particular, nano–sized Au clusters supported on oxides have shown very active behavior for a catalytic reaction like CO oxidation [26–28,47–50]. Many studies showed that catalytic activities of Au nanoclusters strongly depend on their charge states and atomic structures [52–55]. Furthermore, the atomic structures of Au nanoclusters can be also affected by the charge states of the Au species [57,93,94]. In addition to the catalysis of metal nanoclusters, for the growth of thin films and nanostructures on insulating substrates, the highly enhanced kinetics was seen in charged species, as compared with that in charge–neutral species [1].

As a model system to examine charged metal clusters on oxides, in our previous works with *ab–initio* calculations, we theoretically studied the charging effects on the adsorption of Au monomer and dimers on MgO(100), of which charge–neutral systems have been widely studied both experimentally and theoretically [8,99].

In the case of Au monomers [99], the results showed that the most stable adsorption site of Au^+ on MgO(100) was atop the O site, in agreement with that of Au^0. The Au−O bond length was shortened to 2.02 Å as compared with that (2.25 Å) of Au^0.

For Au^- on MgO(100), the most stable adsorption site was atop the Mg site. The Au−Mg bond length was greatly elongated to 2.73 Å as compared with the Au−O bond length (2.25 Å) of Au^0.

In the case of Au dimers [8], the most stable adsorption structure of Au_2^+ on MgO(100) was the upright dimer on a surface O atom, in agreement with that of Au_2^0. The Au−O bond length was shortened to 2.09 Å as compared with that (2.12 Å) of Au_2^0.

For Au_2^- on MgO(100), the most stable adsorption structure was the flat−lying dimer on two surface Mg atoms. The Au−Mg bond length was elongated to 2.83 Å as compared with the Au−O bond length (2.12 Å) of Au_2^0.

The calculation results showed the significant roles of the charge states of Au speices in the resulting structural, physical, chemical, and dynamic properties of Au monomers and dimers on MgO(100).

Despite these studies, experimental information on the charge states and the adsorption structures of Au and Au_2 on MgO(100) remain uncertain. In particular, vibrational measurements are very useful for studying the adsorption of metal nanoclusters on oxides. There have been no experimental or theoretical works on the vibrational properties of charged metal species on oxides.

In this study, the phonon densities of states (ph−DOSs) of charge−neutral and charged Au and Au_2 adsorbed on MgO(100) were studied by conducting *ab−initio* calculations based on the density functional perturbation theory (DFPT). The calculations revealed charge−dependent characteristic features in the ph−DOSs of Au and Au_2 on MgO(100). This could play a significant role in experimentally explaining the charge states of Au species on MgO(100).

6.2. Computational Details

All the calculations were performed using the plane−wave pseudopotential method within the framework of spin−polarized density functional theory (DFT), as implemented in the Vienna Ab−initio Simulation Package (VASP) code [59,60,79,80].. For the exchange−correlation interactions of electrons, the generalized gradient approximation (GGA) functional of Perdew, Burke, and Ernzerhof (PBE) was used[61]. The pseudopotentials for electron−ion interactions were described using the projector augmented−wave (PAW) method [62]. The electronic wave functions were expanded using a plane wave basis set with an energy cutoff of 400 eV. For an

MgO substrate, we used a supercell with a repeating slab structure consisting of 3 MgO layers with a ~15 Å vacuum region along the surface normal direction, and a 3×3 surface unit cell in the lateral (*x* and *y*) directions. The charge-neutral and charged Au species were adsorbed only on the upper side of the slab. A theoretical PBE equilibrium lattice constant (a_0 = 4.24 Å) for bulk MgO was used for the slab. The **k**-point integration was conducted with a 7×7×1 grid in the Brillouin zone (BZ) of the supercell. Geometry optimization was conducted until the remaining forces of the atoms were smaller than 0.01 eV/Å.

To calculate the ph-DOSs for the vibrational spectra of Au_N (N =1, 2) on MgO(100), we used the PHONOPY code, which utilizes the interatomic force constants generated by performing DFPT calculations implemented in VASP [100-102]. A 7×7×1 **q**-point grid was used to calculate the ph-DOSs.

6.3. Results and Discussions

6.3.1. Phonon spectra and modes of Au monomers on MgO(100)

As mentioned earlier, the modst stable adsorption structures of charge-neutral Au (Au^0) and charged Au (Au^+ and Au^-) monomers on MgO(100). The adsorption structures of Au^0, Au^+, and Au^- on

MgO(100) were identified in our previous work with the 4×4 surface unit cell [99]. For Au^0 and Au^+, the surface O site (O_T) was the most stable adsorption site, whereas for Au^-, the surface Mg site (Mg_T) was the most stable adsorption site.

We calculated the phonon spectra from the geometry-optimized structures of clean MgO(100), Au^0, Au^+, and Au^- on MgO(100) in Fig. 6.1. Fig. 6.2 shows the simulated ph-DOSs for clean MgO(100), Au^0, Au^+, and Au^- on MgO(100). Here, the phonon eigenvalues were broadened using a Gaussian function of width 0.4 THz. As a result of the broadening, very small artificial structures of the ph-DOSs in the negative frequency region are formed, but the ph-DOS peak structures are not affected by the artificial structures.

The phonon spectra of the clean MgO(100) surfaces are the projected ph-DOS of the two upper MgO-layer atoms (Mg and O) of the model slab, whereas the projected ph-DOSs of the Au^q (q = 0, +, −) on MgO(100) also include the adsorbed Au adatom (see black lines in Fig. 6.2.)

For clean MgO(100), the ph-DOS shows intense broad band in the region of 4-18 THz with three peaks located at 8.32, 11.65, and 16.03 THz, respectively [Fig. 6.2 (a)].

For Au^q on MgO(100), the ph-DOSs show a weak band with two peaks in the region below 4 THz and an intense broad band with three peaks in the region of 4–18 THz, which are similar to those of clean MgO(100) (see Fig. 6.2).

For Au^0, the peak positions are located at 0.45 and 1.90 THz for the lower weak band and at 8.38, 11.56, and 16.05 THz for the higher intense broad band. For Au^+, the peak positions are located at 0.55 and 1.60 THz for the lower weak band and at 8.31, 11.73, and 16.20 THz for the higher intense broad band. For Au^-, the peak positions are located at 0.34 and 1.55 THz for the lower weak band and at 8.11, 11.73, and 16.01 THz for the higher intense broad band.

To obtain more detailed information on phonon spectra, we also investigated the atom-projected vibrations of the adsorbed Au atom and of the Mg and the O atoms in the two topmost surface MgO layers. In Fig. 6.2, the Au-projected modes are indicated by the red line. The Mg- and the O-projected modes are indicated by the green and blue lines, respectively.

For clean MgO(100), the ph-DOS band in the range of 4–10 THz consists mainly of the Mg modes. The ph-DOS band in the range of 10–14 THz consists of a mixture of the Mg and O modes. The ph-DOS band in the range of 14–18 THz consists mainly of the O modes. The Mg-projected surface vibrational modes have three phonon peaks at 8.19, 11.25, and 16.43 THz. The O-projected surface vibrational modes have two phonon peaks at 12.18, and 15.90 THz.

For Au^0, Au^+, and Au^- on MgO(100), the lower weak band with two peaks in the region below 4 THz consists mainly of the Au modes and is clearly distinguishable from that of clean MgO(100). The upper intense broad band with three peaks in the region of 4-18 THz mainly consists of the Mg and O modes which are similar to those of clean MgO(100).

For Au^0, the Au-projected vibrational modes have two peaks at 0.45 and 2.03 THz. The Mg-projected surface vibrational modes have three peaks at 8.25, 11.29, and 16.32 THz. The O-projected surface vibrational modes have two peaks at 12.09 and 15.92 THz.

For Au^+, the Au-projected vibrational modes have one peak at 0.55 THz that is different from that of Au^0. The Mg-projected surface vibrational modes have three peaks at 8.05, 11.34, and 16.33 THz. The O-projected surface vibrational modes have two peaks at 11.99 and 16.07 THz.

For Au^-, the Au-projected vibrational modes have one peak at 0.34 THz that is different from that of Au^0. The Mg-projected surface vibrational modes have three peaks at 8.11, 11.19, and 15.89 THz. The O-projected surface vibrational modes have two peaks at 12.00 and 15.89 THz.

For more detailed analysis of the vibrational features associated with the most stable adsorption structures of Au^0, Au^+, and Au^- on

MgO(100), we also investigated the surface in−plane and normal vibrations of the Au monomers. Fig. 6.3 shows the enlarged ph−DOSs in the region below 4 THz with the Au−projected ph−DOSs of the surface in−plane and normal vibrational modes. Here, the surface in−plane and normal modes are indicated by the orange and purple lines, respectively.

For Au^0, Au^+, and Au^-, the lower peak of the weak band in the region 0−1 THz mainly consists of the surface in−plane modes. The surface in−plane ph−DOSs of Au show the peak positions at 0.45 (Au^0), 0.55 (Au^+), and 0.34 THz (Au^-). This shows that hardening (softening) in the surface in−plane modes occurs for positive (negative) charging of Au.

For Au^0, Au^+, and Au^-, the upper peak of the weak band in the region 1−3 THz mainly consists of the surface normal modes. The surface normal ph−DOSs of Au show the peak positions at 2.03 (Au^0), 1.60 (Au^+), and 1.55 THz (Au^-). This shows that softening in the surface normal modes occurs for both positive and negative charging of Au.

Next, we investigated the frequencies and corresponding representations of surface vibrational modes for the most stable adsorption structures of Au^0, Au^+, and Au^- on MgO(100) surfaces. Their vibrational assignments are presented in Table 6.1, and the vibrations are described in Fig. 6.4.

In the case of Au^0 on MgO(100), the lower phonon band of the surface in-plane modes in the region below 1 THz has a frustrated translation-1 mode at 0.50 THz. This mode is illustrated in Fig. 6.4(a). In the frustrated translation-1 mode, the Au atom at the O_T site vibrates in surface in-plane (x and y) directions by bending the Au-O_s bond towards the surface H sites. The phonon band of the surface normal mode in the region 1-3 THz has a stretching-1 mode at 2.09 THz. This mode is illustrated in Fig. 6.4(b). In the stretching-1 mode, the Au and the nearest O_s atoms move up and down in phase with each other along the z direction. The vibrational amplitude of the Au atom is larger than that of the O_s atom. This mode shows the stretching characteristics of the Au-O_s and O_s-Mg_{ss} bonds.

In the case of Au^+ on MgO(100), the lower phonon band of the surface in-plane modes in the region 0-1 THz has a frustrated translation-1 mode at 0.57 THz, which is higher by 0.07 THz than that of Au^0 on MgO(100). This mode is illustrated in Fig. 6.4 (c). Hardening in this surface in-plane phonon spectrum is coincident with shortening to 2.01 Å in the Au-O_s bond length induced by the positive charging of Au as compared with that (2.26 Å) of Au^0. The phonon band of the surface normal mode in the region 1-3 THz has a stretching-1 mode at 1.80 THz, which is lower by 0.29 THz than that of Au^0 on MgO(100). This mode is illustrated in Fig. 6.4 (d).

Softening in this surface normal phonon spectrum is coincident with the structural changes induced by the positive charging of Au, where the O_s−Mg_{ss} bond length is elongated to 2.54 Å as compared with that (2.17 Å) of Au^0.

In the case of Au^-, the lower phonon band of the surface in−plane modes in the region 0−1 THz has a frustrated translation−2 mode at 0.37 THz, which is lower by 0.13 THz than that of the frustrated translation−1 mode of Au^0. This mode is illustrated in Fig. 6.4(e). Softening in this surface in−plane phonon spectrum is coincident with elongating to 2.73 Å in the Au−Mg_s bond length induced by the negative charging of Au as compared with that (2.26 Å) of the Au−O_s bond of Au^0. In the frustrated translation−2 mode,

the Au atom at the Mg_T site vibrates in surface in−plane directions by bending the Au−Mg_s bond towards the surface *H* sites. The phonon band of the surface normal mode in the region 1−3 THz has a stretching−2 mode at 1.57 THz, which is lower by 0.52 THz than that of the stretching−1 mode of Au^0. This mode is illustrated in Fig. 6.4(f). In the stretching−2 mode, the Au and Mg_s atoms move up and down in phase with each other along the *z* direction. The vibrational amplitude of the Au atom is larger than that of the Mg_s atom. Softening in this surface normal phonon spectrum is coincident with the structural changes induced by the negative charging of Au, where the Mg_s–O_{ss} bond length is elongated to 2.41 Å compared with the O_s–Mg_{ss} bond length (2.17 Å) of Au^0.

6.3.2. Phonon spectra and modes of Au dimers on MgO(100)

Next, we carried out vibrational spectra calculations for charge-neutral Au_2 (Au_2^0) and charged Au_2 (Au_2^+ and Au_2^-) on MgO(100). The modst stable adsorption structures of Au_2^0, Au_2^+, and Au_2^- on MgO(100) were identified in our previous work [8]. For Au_2^0 and Au_2^+, the upright dimer structure (S_O) on top of the surface O atom was the most stable. For Au_2^-, the flat-lying dimer structure ($P_{\mathrm{Mg-H-Mg}}$) on top of two surface Mg atoms was the most stable.

We calculated the phonon spectra from the geometry-optimized structures of Au_2^0, Au_2^+ and Au_2^- on MgO(100) with their most stable adsorption structures in Fig 6.5. Fig. 6.6 shows the simuated ph-DOSs for Au_2^0, Au_2^+ and Au_2^- on MgO(100), where the phonon eigenvalues were broadened using a Gaussian function of width 0.4 THz.

In Fig. 6.6, the projected ph-DOSs of the two upper MgO-layer (Mg and O) and Au dimer atoms are indicated by black lines.

The ph-DOSs of Au_2^0, Au_2^+, and Au_2^- on MgO(100) in Fig 6.6 (a), (b), and (c) show a weak band in the region below 5 THz and an intense broad band with three peaks in the region 5–18 THz, which are similar to those of clean MgO(100) in Fig. 6.2 (a). For Au_2^0, the peak positions are located at 0.18 and 1.64 THz for the lower weak band and at 8.40, 11.57, and 16.07 THz for the higher intense broad band. For Au_2^+, the peak positions are located at 0.25 and 1.49 THz for the lower weak band and at 8.53, 11.50, and 15.46 THz for the higher intense broad band. For Au_2^-, the peak positions are located at 0.28 and 3.95 THz for the lower weak band and at 8.01, 11.54, and 16.01 THz for the higher intense broad band.

To obtain more detailed information on phonon spectra, we also investigated the atom–projected vibrations of the adsorbed Au atoms and of the Mg and the O atoms in the two topmost surface MgO layers for the most stable adsorption structures of Au_2^q on MgO(100). In Fig. 6.6, the Au–projected modes are indicated by the red line. The Mg– and O– projected modes are indicated by the green and blue lines, respectively.

As with the results of Au monomers, the ph–DOSs of Au_2^0, Au_2^+, and Au_2^- on MgO(100) show that the lower weak band in the region below 4 THz mainly consists of the Au modes and that the upper intense broad band with three peaks in the range of 4–18 THz mainly consists of the Mg and O modes, which is similar to that of clean MgO(100) in Fig. 6.2.

For Au_2^0, the Au-projected vibrational modes have three peaks at 0.18, 1.51, and 5.48 THz. The Mg-projected surface vibrational modes have three peaks at 8.13, 11.30, and 16.47 THz. The O-projected surface vibrational modes have two peaks at 12.10 and 15.94 THz.

For Au_2^+, the Au-projected modes have three peaks at 0.25, 1.37, and 5.20 THz. The Mg-projected surface vibrational modes have three peaks at 8.29, 11.26, and 15.46 THz. The O-projected surface vibrational modes have two peaks at 11.87 and 15.46 THz.

For Au_2^-, the Au-projected modes have two peaks at 0.28 and 4.08 THz. The Mg-projected surface vibrational modes have three peaks at 8.01, 11.26, and 16.28 THz. The O-projected surface vibrational modes have two peaks at 12.08 and 15.88 THz.

For more detailed analysis of the vibrational features associated with the most stable adsorption structures of Au_2^0, Au_2^+, and Au_2^- on MgO(100), we also investigated the surface in-plane and normal vibrations of the Au dimers. Fig 6.7 shows the enlarged ph-DOSs in the region below 8 THz with the Au-projected ph-DOSs of the surface in-plane and normal vibrational modes. Here, the surface in-plane and normal modes are indicated by the orange and purple lines, respectively.

For Au_2^0 and Au_2^+, the lower peak of the weak band in the region

0-1 THz mainly consists of the surface in-plane modes of Au. The upper peak of the weak band in the region 1-3 THz consists of a mixture of the surface in-plane and normal modes of Au. Another peak of the surface normal mode of Au is located within the ph-DOS in the region above 4 THz which mainly consists of the MgO surface vibrational modes.

For Au_2^0, the surface in-plane ph-DOS of Au shows two peaks at 0.18 and 1.64 THz. The surface normal ph-DOS of Au shows two peaks at 1.37 and 5.48 THz. For Au_2^+, the surface in-plane ph-DOS of Au shows two peaks at 0.25 and 1.49 THz. The surface normal ph-DOS of Au shows two peaks at 1.24 and 5.20 THz.

For Au_2^-, the lower peak of the weak band in the region 0-2 THz consists of a mixture of the surface in-plane and normal modes of Au. The upper peak of the weak band in the region 3-5 THz mainly consists of the surface in-plane modes of Au. The surface in-plane ph-DOS of Au shows two peaks at 0.28 and 4.08 THz. The surface normal ph-DOS of Au shows one peak at 1.23 THz.

Next, we investigated the frequencies and corresponding representations of surface vibrational modes for the most stable adsorption structures of Au_2^0, Au_2^+, and Au_2^- on MgO(100) surfaces. Their vibrational assignments are presented in Table 6.2, and the vibrations are described in Fig. 6.8.

In the case of Au_2^0 on MgO(100), the lower phonon band of the surface in−plane mode in the region below 1 THz has a frustrated translation mode at 0.18 THz. This mode is illustrated in Fig. 6.8(a). In the frustrated translation mode, the Au dimer atoms move in phase in the *x* (*y*) direction. The vibrational amplitude of the upper dimer atom (Au2) is larger than that of the lower dimer atom (Au1).

The ph−DOS band of the surface in−plane mode in the region 1−3 THz has a frustrated rotation mode at 1.70 THz. In the frustrated rotation mode, the Au1 and Au2 atoms move out of phase in the *x* (*y*) direction. The vibrational amplitude of Au1 is larger than that of Au2. The ph−DOS band of the surface normal mode in the region 1−3 THz has a stretching−3 mode at 1.64 THz. In the stretching−3 mode, the Au1 and Au2 atoms move in phase in the *z* direction.

The ph−DOS band of the surface normal mode in the region 4−6 THz has a stretching−4 mode at 5.49 THz. In the stretching−4 mode, the Au1 and Au2 atoms move out of phase in the *z* direction by stretching the Au1−Au2 bond.

In the case of Au_2^+ on MgO(100), the lower phonon band of the surface in−plane mode in the region below 1 THz has a frustrated translation mode as in Au_2^0. The frequency of the frustrated translation mode is 0.29 THz, which is higher by 0.11 THz than that of Au_2^0. This mode is illustrated in Fig. 6.8(e). Hardening in this surface in−plane phonon spectrum is coincident with shortening to 2.10 Å in the Au1−O_s bond length induced by the positive charging of Au_2 as compared with that (2.14 Å) of Au_2^0 [see Fig. 6.8(e) and (a)].

The ph−DOS band of the surface in−plane mode in the region 1−3 THz has a frustrated rotation modes as in Au_2^0. The frequency of the frustrated rotation mode is 1.54 THz, which is lower by 0.16 THz than that of Au_2^0. This mode is illustrated in Fig. 6.8(f).

The ph−DOS band of the surface normal mode in the region 1−3 THz has a stretching−3 modes as in Au_2^0. The frequency of the stretching−3 mode is 1.55 THz, which is lower by 0.09 THz than that of Au_2^0. This mode is illustrated in Fig. 6.8(g).

The ph−DOS band of the surface normal mode in the region 4−6 THz has a stretching−4 mode as in Au_2^0. The frequency of the stretching−4 mode is 5.20 THz, which is lower by 0.29 THz than that of Au_2^0. This mode is illustrated in Fig. 6.8(h). Softening in these surface normal phonon spectra (stretching−3, 4) is coincident with the structural changes induced by positive charging of Au_2, where the O_s−Mg_{ss} bond length is elongated to 2.28 Å as compared with that (2.21 Å) of Au_2^0.

In the case of Au_2^-, the lower phonon band of the surface in−plane mode in the region below 1 THz has frustrated rotation−*z*, frustrated translation−*y*, frustrated translation−*x* modes at 0.24, 0.29, and 0.41 THz, respectively. These modes are illustrated in Fig. 6.8(i), (j), and (k), respectively. In the frustrated rotation−*z* mode, the two Au atoms move out of phase in the *y* direction. The rotational axis is the *z*−axis at the dimer bond center. In the frustrated translation−*y* mode, the two Au atoms move in phase in the *y* direction. In the frustrated translation−*x* mode, the two Au atoms move in phase in the *x* direction.

The ph−DOS band of the surface in−plane mode in the region in 3−5 THz has a stretching−*x* mode at 4.02 THz. This mode is illustrated in Fig. 6.8(l). In the stretching−*x* mode, the two Au atoms move out of phase in the *x* direction. The ph−DOS band of the surface normal modes in the region 1−2 THz has frustrated rotation−*y* and stretching−*z* modes at 1.22 and 1.43 THz, respectively. These modes are illustrated in Fig. 6.8(m) and (n), respectively. In the frustrated rotation−*y* mode, the two Au atoms move out of phase in the *z* direction. The rotational axis is the *y*−axis at the dimer bond center. In the stretching−*z* mode, the two Au atoms move in phase in the *z* direction.

6.4. Conclusion

Performing DFPT calculations, we investigated the ph−DOSs of Au and Au_2 with different charge states on MgO(100) surfaces. For Au monomers, the ph−DOSs showed a weak band in the region below 4 THz and an intense broad band in the region 4−18 THz.

For Au dimers, the ph−DOSs showed a weak band in the region below 5 THz and an intense broad band in the region 5−18 THz.

The weak band and intense broad bands are associated with the modes of the Au atoms and of the surface MgO−layer atoms, respectively, for all three different charge states.

To extract the vibrational features associated with the adsorption structures of Au and Au_2 with different charge states on MgO(100), we also investigated in detail the frequencies and corresponding representations of the surface in−plane and normal vibrations of the weak bands of the Au atoms. The calculation results clearly showd charge−dependent characteristic features in the surface vibrational spectra of Au and Au_2 on MgO(100).

The vibrational changes with the adsorption of Au and Au_2 on MgO(100) agreed well with the structural changes induced by the charging. The differences in the ph−DOSs obtained in this study are expected to provide fundamentally important information for experimentally explaining charge states of Au and Au_2 on MgO(100), hich has yet to be addressed.

This study is a step forward in research for understanding the physics and chemistry of charged metal nanoclusters on oxides.

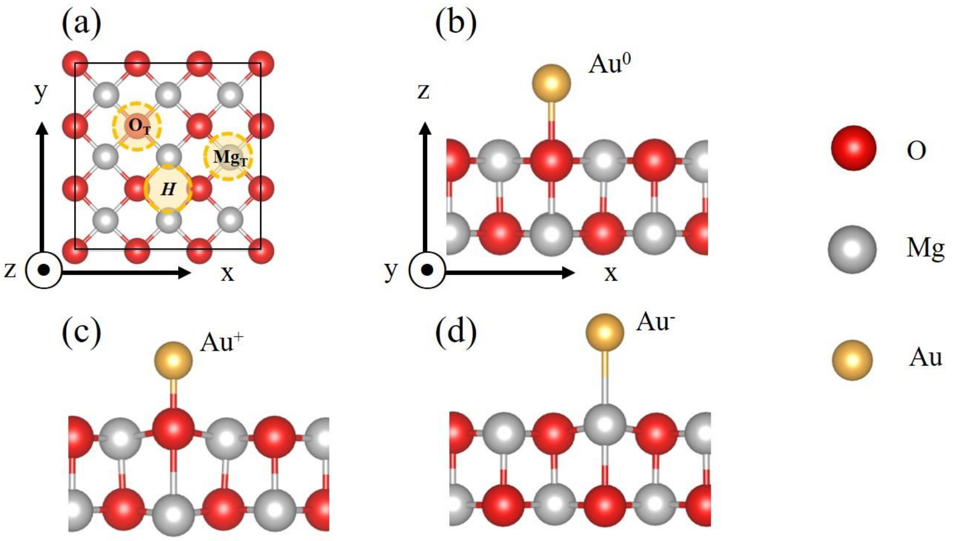

Figure 6.1 Top view of clean MgO(100) and side views of the geometry-optimized adsorption structures of the charge-neutral and charged Au adatoms on MgO(100): (a) Clean MgO(100), (b) Au^0 on top of a surface O atom of MgO(100), (c) Au$^+$ on top of a surface O atom of MgO(100), and (d) Au$^-$ on top of a surface Mg atom of MgO(100). The black lines in (a) denote the 3×3 surface unit cell used in the calculations.

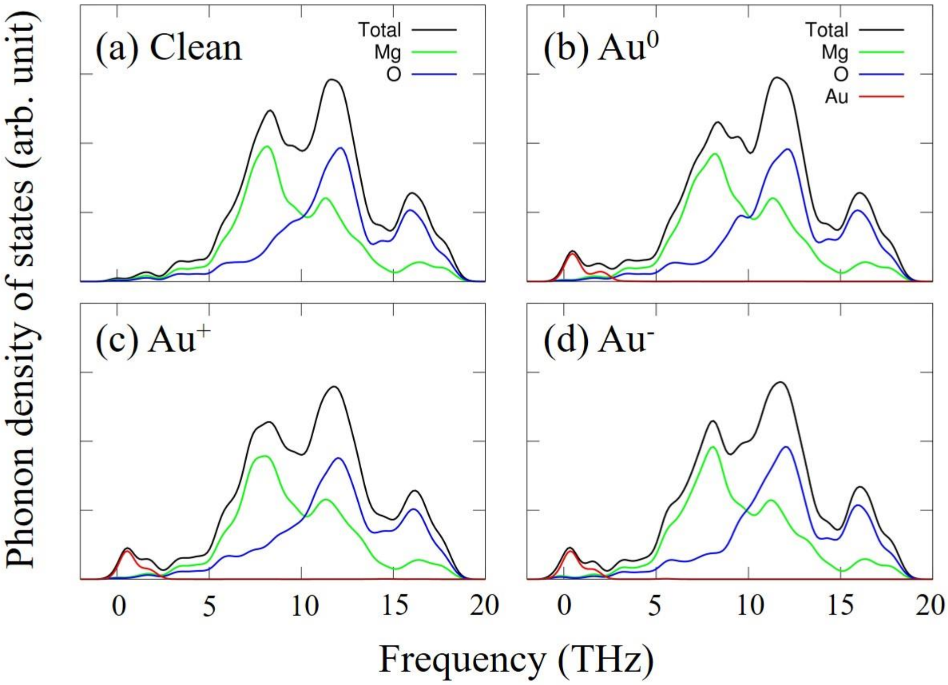

Figure 6.2 Calculated surface phonon densities of states (ph−DOSs) of clean MgO(100) and Au^q (q = 0, +, −) on MgO(100): (a) Clean MgO(100), (b) Au^0 , (c) Au$^+$, and (d) Au$^-$. The black lines represent the surface ph−DOSs of clean MgO(100) and Au^q on MgO(100). Here, the phonon spectra of clean MgO(100) are the projected ph−DOSs of the two upper MgO−layer atoms (Mg and O), whereas the phonon spectra of Auq on MgO(100) also include the adsorbed Au adatoms. The green and blue lines represent the Mg− and O−projected vibrational modes of the two topmost MgO−layer atoms, respectively. The red line represents the Au−projected vibrational modes. In the calculations, the phonon eigenvalues were broadened using a Gaussian function of width 0.4 THz.

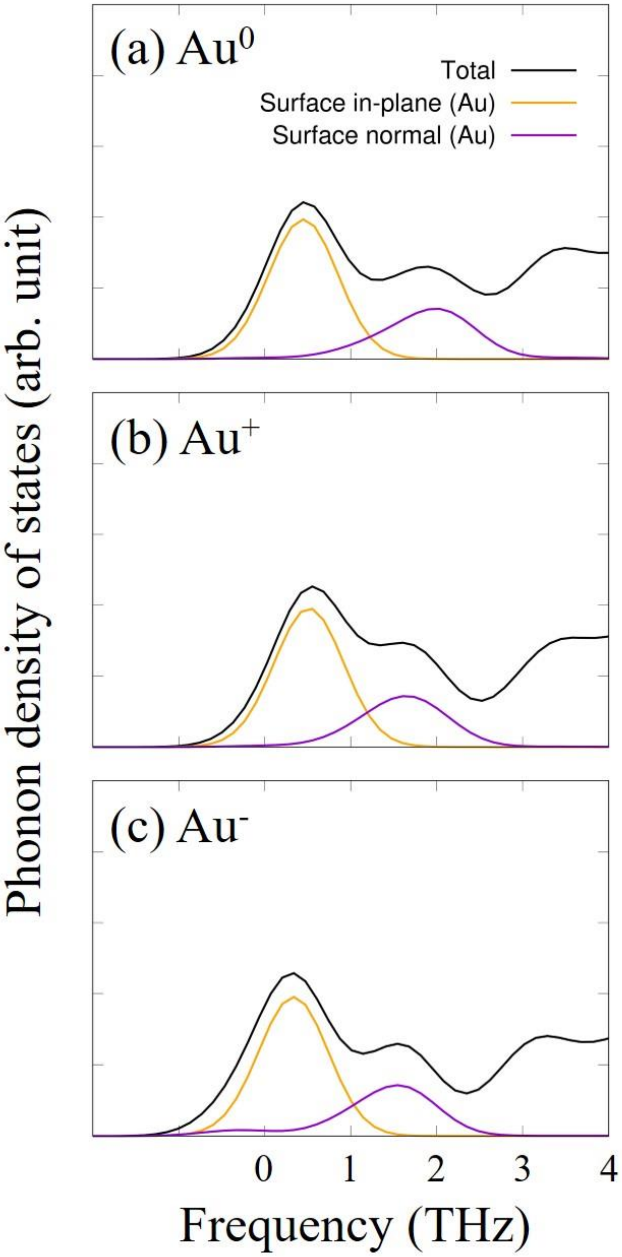

Figure 6.3 Enlarged ph−DOs bands in the region below 5 THz for Au^q (q = 0, +, −) on MgO(100): (a) Au^0, (b) Au$^+$, and (c) Au$^-$. The black solid line represents the projected ph−DOSs of the two upper MgO−layer atoms (Mg and O atoms) and adsorbed Au atoms. The orange and the purple lines represent the surface in−plane and the surface normal vibrational modes of the adsorbed Au atoms, respectively. In the calculations, the phonon eigenvalues were broadened using a Gaussian function of width 0.4 THz.

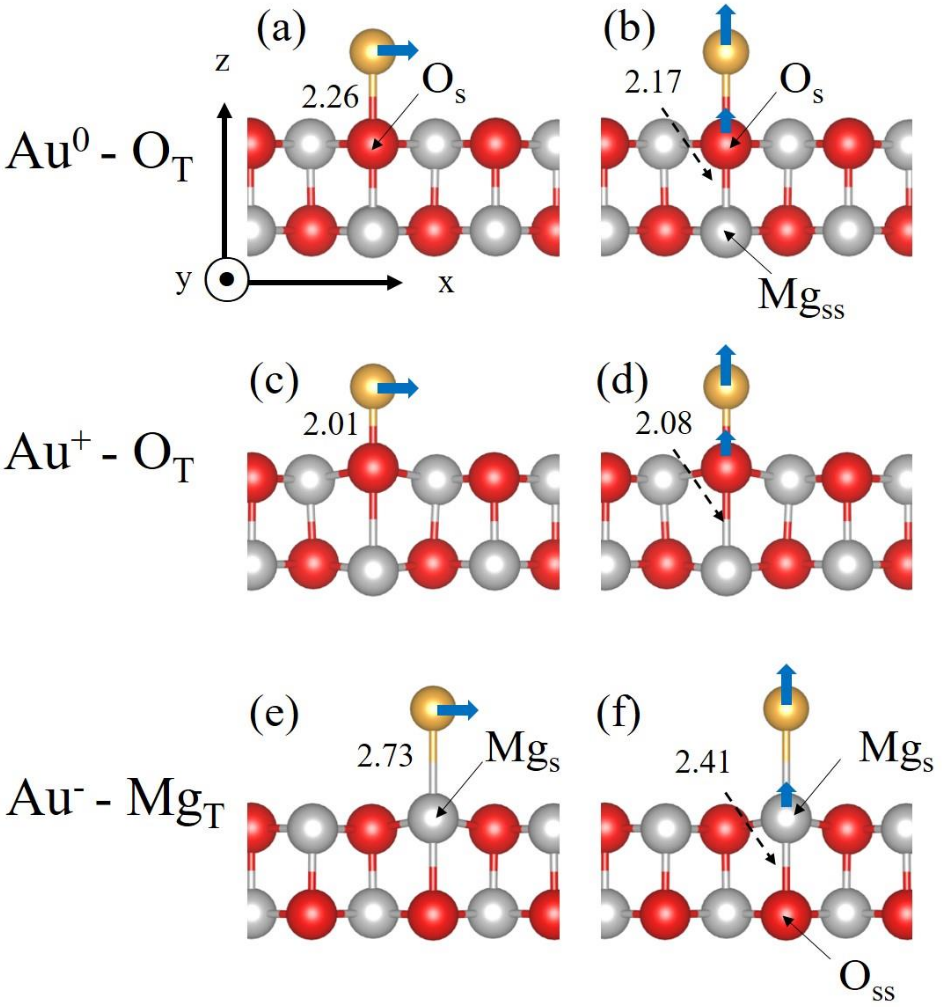
(a)
z
Au^0 - O_T
2.26
O_s
y
x
(b)
2.17
O_s
Mg_{ss}
(c)
Au^+ - O_T
2.01
(d)
2.08
(e)
Au^- - Mg_T
2.73
Mg_s
(f)
2.41
Mg_s
O_{ss}

Figure 6.4 Representations of the surface in−plane [(a), (c), and, (e)] and the surface normal [(b), (d), and (f)] phonon modes for the most stable adsorption structures of Au^q on MgO(100) structures, corresponding to the selected frequencies in Table 1. Blue arrows indicate the amplitude and direction for each atom in each phonon mode. (a) Frustrated translation−1 mode of Au^0 (b) Stretching−1 mode of Au^0 , (c) Frustrated translation−1 mode of Au^+, (d) Stretching−1 of Au^+, (e) Frustrated translation−2 mode of Au^-, and (f) Stretching−2 of Au^- . The numbers for Au^0 and Au^+ (Au^-) on MgO(100) represent the interatomic distances between O_s (Mg_s) and its neighboring atoms in Å.

Table 6.1 Calculated frequencies and corresponding representations of surface phonon modes for the most stable adsorption structures of Au^q (q=0, +, −) on MgO(100)

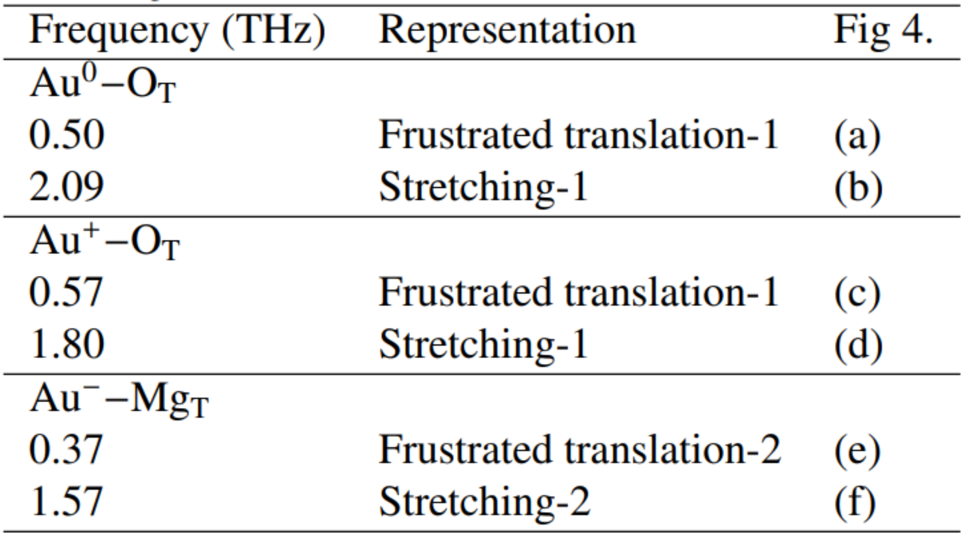

Frequency (THz)	Representation	Fig 4.
Au^0–O_T		
0.50	Frustrated translation-1	(a)
2.09	Stretching-1	(b)
Au^+–O_T		
0.57	Frustrated translation-1	(c)
1.80	Stretching-1	(d)
Au^-–Mg_T		
0.37	Frustrated translation-2	(e)
1.57	Stretching-2	(f)

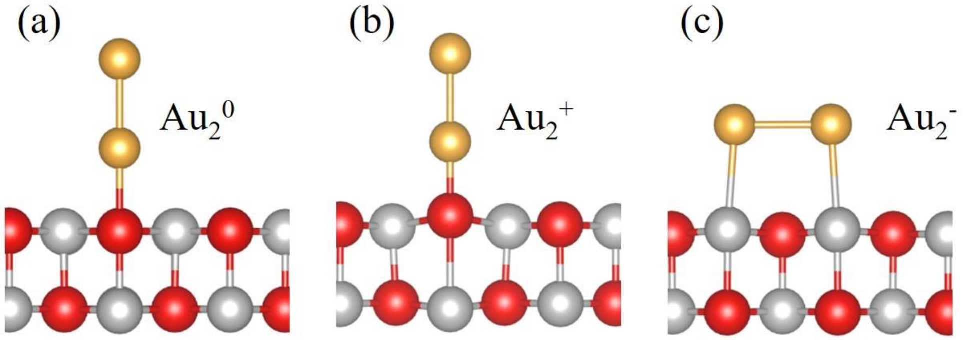

Figure 6.5 Side views of the geometry-optimized adsorption structures of Au_2^q on MgO(100): (a) Upright Au_2^0 (Au_2^0-S_O), (b) upright Au_2^+ (Au_2^+-S_O) on top of a surface O atom of MgO(100), and (c) flat-lying Au_2^- (Au_2^--$P_{Mg-H-Mg}$) on top of two surface Mg atoms of MgO(100).

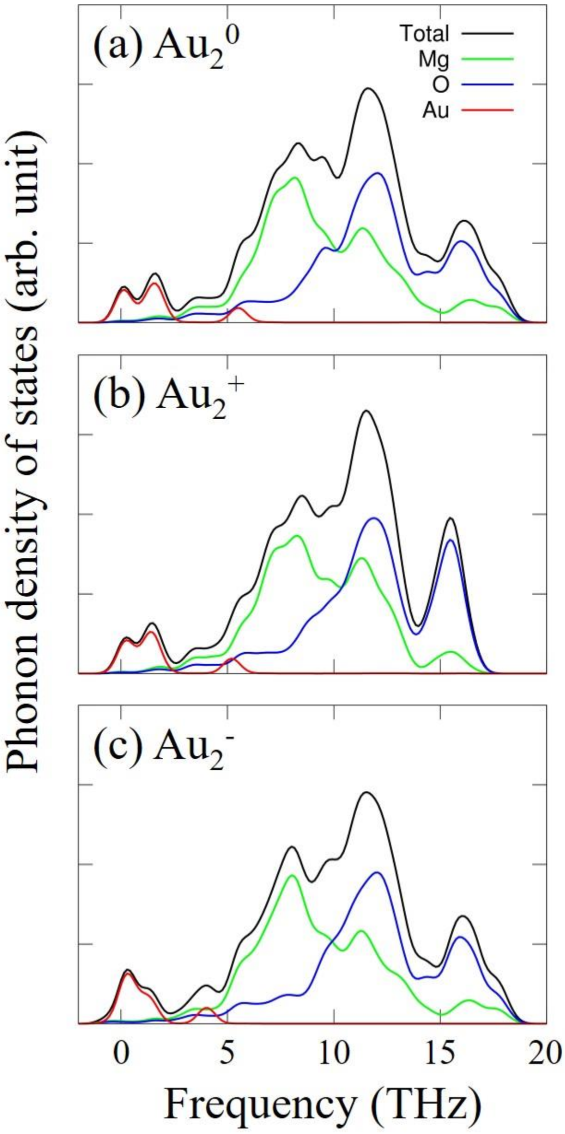

Figure 6.6 Calculated ph−DOSs of Au_2^q (q = 0, +, −) on MgO(100): (a) Au_2^0 $-S_O$, (b) $Au_2^+$$-S_O$, and (c) Au_2^- $-P_{Mg-H-Mg}$. The black line represents the surface ph−DOSs of Au_2^q on MgO(100). Here, the phonon spectra of Au_2^q on MgO(100) also show the projected ph−DOSs of the two upper MgO−layer atoms (Mg and O) and adsorbed Au_2 atoms. The green and blue lines represent the Mg− and O−projected vibrational modes of the two topmost MgO−layer atoms, respectively. The red line represents the vibrational modes of adsorbed Au2 atoms. In the calculations, the phonon eigenvalues were broadened using a Gaussian function of width 0.4 THz.

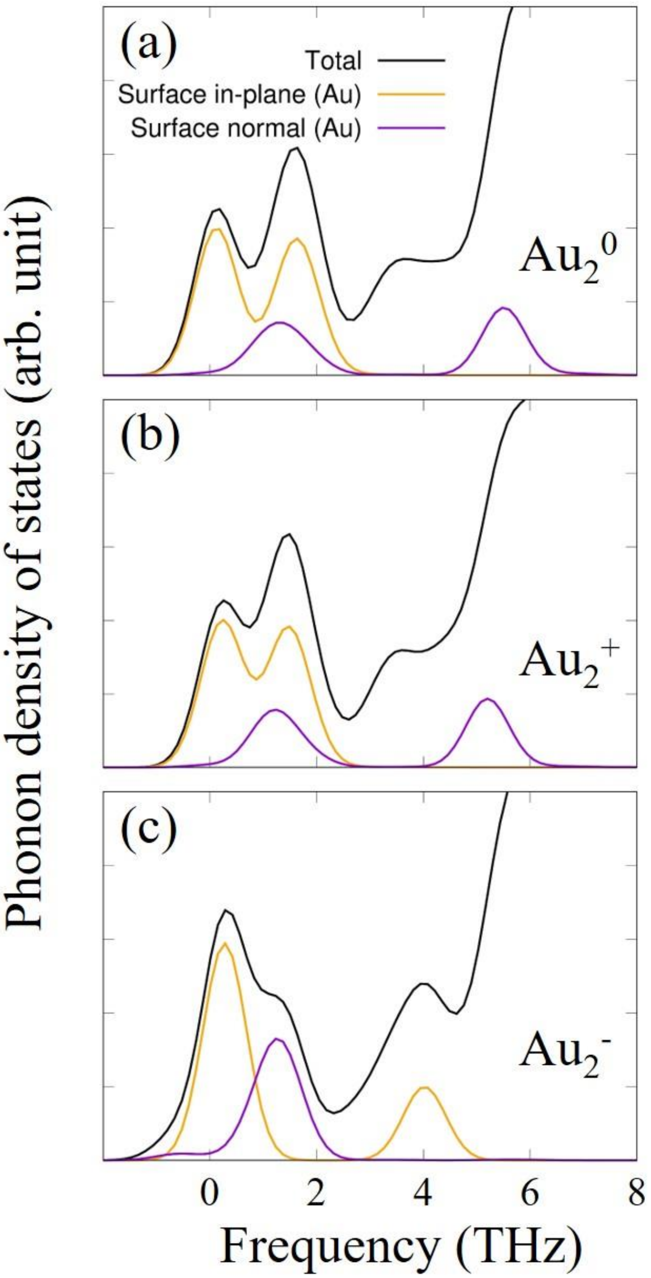

Figure 6.7 Enlarged ph−DOSs bands in the region below 8 THz for $Au_2{}^q$ (q = 0, +, −) on MgO(100): (a) $Au_2{}^0$ −S_O, (b) $Au_2{}^+$−S_O, and (c) $Au_2{}^-$ −$P_{Mg-H-Mg}$. The black solid line represents the projected ph−DOSs of the two upper MgO−layer atoms (Mg and O) and adsorbed Au2 atoms. The orange and the purple lines represent the surface in−plane and the surface normal vibrational modes of the adsorbed Au_2 atoms, respectively. In the calculations, the phonon eigenvalues were broadened using a Gaussian function of width 0.4 THz.

Table 6.2 Calculated frequencies and corresponding representations of surface phonon modes for the most stable adsorption structures of Au_2^q (q = 0, +, −) on MgO(100).

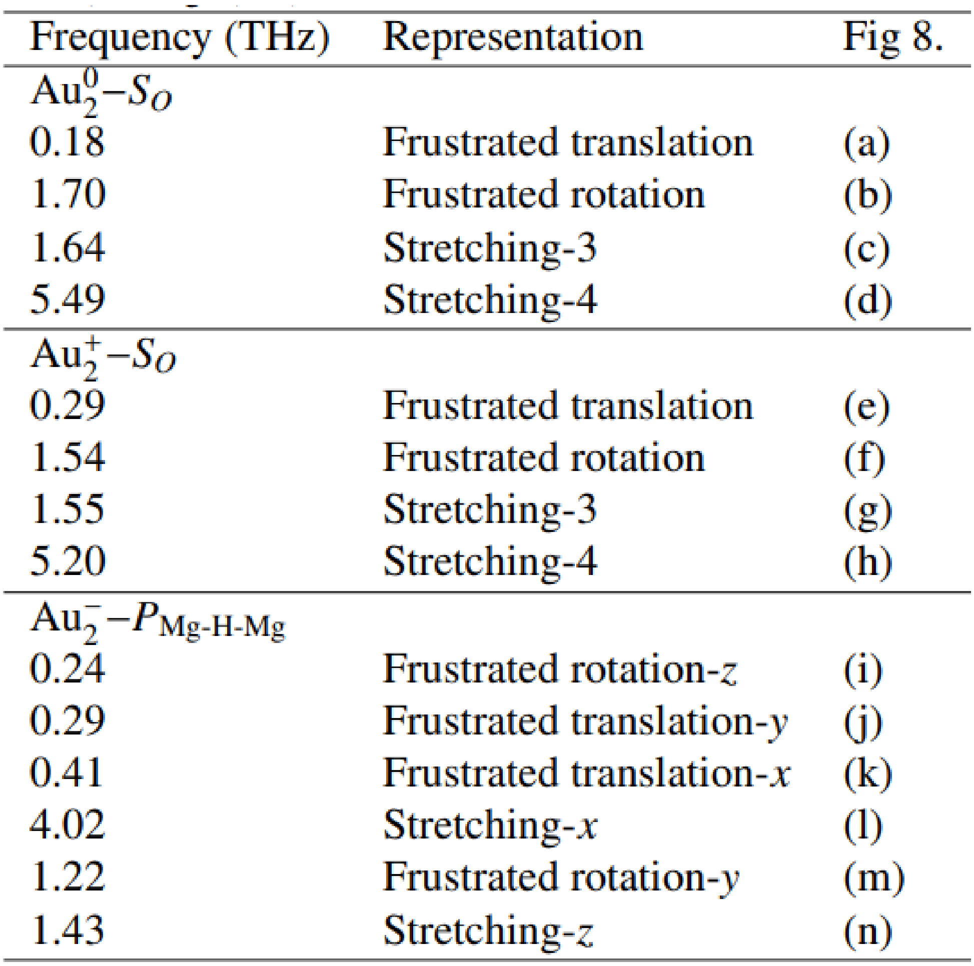

Frequency (THz)	Representation	Fig 8.
$Au_2^0-S_O$		
0.18	Frustrated translation	(a)
1.70	Frustrated rotation	(b)
1.64	Stretching-3	(c)
5.49	Stretching-4	(d)
$Au_2^+-S_O$		
0.29	Frustrated translation	(e)
1.54	Frustrated rotation	(f)
1.55	Stretching-3	(g)
5.20	Stretching-4	(h)
$Au_2^--P_{\text{Mg-H-Mg}}$		
0.24	Frustrated rotation-z	(i)
0.29	Frustrated translation-y	(j)
0.41	Frustrated translation-x	(k)
4.02	Stretching-x	(l)
1.22	Frustrated rotation-y	(m)
1.43	Stretching-z	(n)

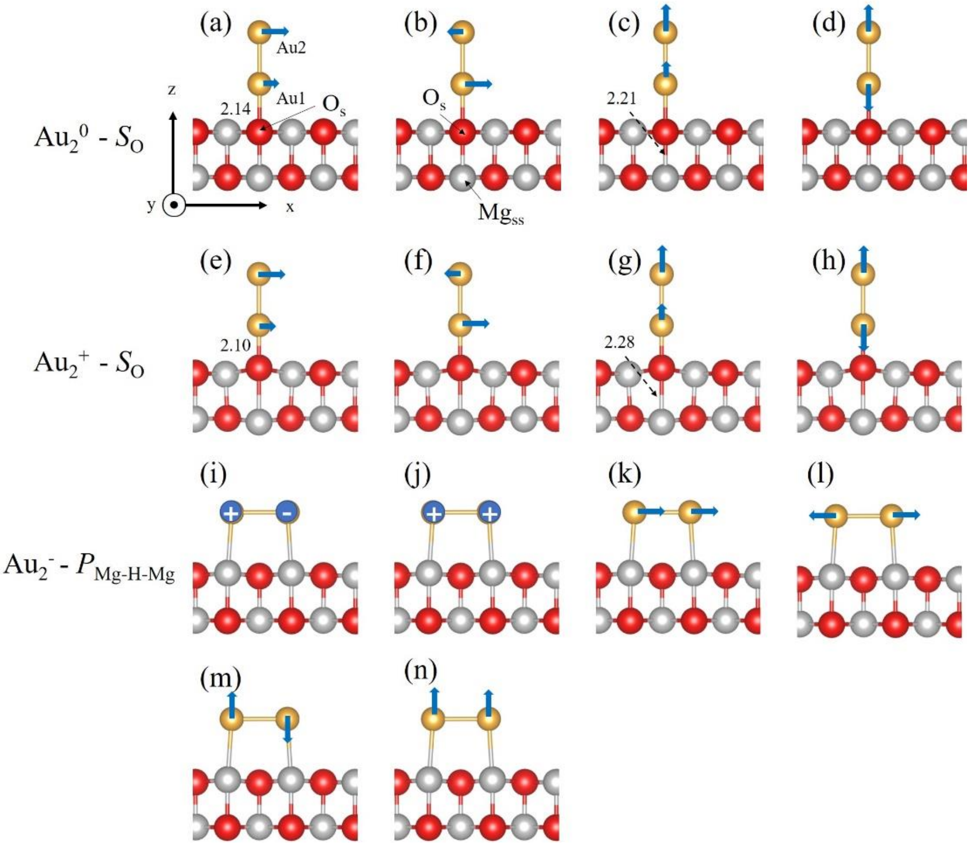

Figure 6.8 Representations of the surface in−plane [(a), (b), (e), (f), (i), (j), (k), and (l)] and the surface normal [(c), (d), (g), (h), (m), and (n)] phonon modes for the most stable adsorption structures of Au_2^q on MgO(100), corresponding to the selected frequencies in Table 2. Arrows indicate the amplitude and direction for each atom in each phonon mode. (a) Frustrated translation of Au_2^0, (b) frustrated rotation of Au_2^0, (c) stretching−3 of Au_2^0, (d) stretching−4 of Au_2^0, (e) frustrated translation of Au_2^+, (f) frustrated rotation of Au_2^+, (g) stretching−3 of Au_2^+, (h) stretching−4 of Au_2^+, (i) frustrated rotation−z of Au_2^-, (j) frustrated translation−y of Au_2^-, (k) frustrated translation−x of Au Au_2^-, (l) stretching−x of Au_2^-. (m) frustrated rotation−y of Au_2^-, and (n) stretching−z of Au_2^-. The numbers for Au_2^0 and Au_2^+ on MgO(100) represent the interatomic distances between O_s and its neighboring atoms in Å.

Bibliography

[1] N. M. Hwang, *Non-Classical Crystallization of Thin Films and Nanostructures in CVD and PVD Processes* (Springer Netherlands, 2016), Springer Series in Surface Sciences.

[2] W. K. Youn, S. S. Lee, J. Y. Lee, C. S. Kim, N. M. Hwang, and S. Iijima, Journal of Physical Chemistry C **118**, 11946 (2014).

[3] H. Zheng, Y. Liu, S. X. Mao, J. Wang, and J. Y. Huang, Sci Rep **2**, 542 (2012).

[4] K. Zheng *et al.*, Nature Communications **1**, 24 (2010).

[5] S.-w. Park, Y.-k. Ahn, Y.-k. Jeong, T.-w. Na, and N.-m. Hwang, Mater. Charact. **163**, 110235 (2020).

[6] S.-W. Park, G.-S. Jang, K.-S. Kim, and N.-M. Hwang, Electronic Materials Letters **16**, 72 (2020).

[7] J. H. Park, J. W. Yang, M. G. Byun, N. M. Hwang, J. Park, and B. D. Yu, Journal of the Physical Society of Japan **90**, 034602 (2021).

[8] J. H. Park, J. W. Yang, M. G. Byun, N. M. Hwang, J. Park, and B. D. Yu, Current Applied Physics **24**, 39 (2021).

[9] Y. Shen, H. Wang, and Q. An, ACS Applied Electronic Materials **2**, 56 (2020).

[10] M.-J. Kim, K. Lee, K. H. Oh, I.-S. Choi, H.-H. Yu, S.-T. Hong, and H. N. Han, Scripta Materialia **75**, 58 (2014).

[11] H.-J. Jeong, M.-J. Kim, J.-W. Park, C. D. Yim, J. J. Kim, O. D. Kwon, P. P. Madakashira, and H. N. Han, Materials Science and Engineering: A **684**, 668 (2017).

[12] H.-y. Xie, Q. Wang, F. Peng, K. Liu, X.-h. Dong, and J.-f. Wang, Transactions of Nonferrous Metals Society of China **25**, 2686 (2015).

[13] Z.-j. Wang and H. Song, J. Alloy. Compd. **470**, 522 (2009).

[14] Y. H. Zhu, S. To, W. B. Lee, X. M. Liu, Y. B. Jiang, and G. Y. Tang, Materials Science and Engineering: A **501**, 125 (2009).

[15] M.-J. Kim, M.-G. Lee, K. Hariharan, S.-T. Hong, I.-S. Choi, D. Kim, K. H. Oh, and H. N. Han, International Journal of Plasticity **94**, 148 (2017).

[16] J.-W. Park, H.-J. Jeong, S.-W. Jin, M.-J. Kim, K. Lee, J. J. Kim, S.-T. Hong, and H. N. Han, Materials Characterization **133**, 70 (2017).

[17] S. W. Park, J. S. Jung, K. S. Kim, K. H. Kim, and N. M. Hwang, Crystal Growth & Design **18**, 5816 (2018).

[18] S. W. Park, Y. K. Ahn, Y. K. Jeong, T. W. Na, and N. M. Hwang, Materials Characterization **163**, 6, 110235 (2020).

[19] S. W. Park, G. S. Jang, K. S. Kim, and N. M. Hwang, Electronic Materials Letters **16**, 72 (2020).

[20] S. Iijima and T. Ichihashi, Physical Review Letters **56**, 616 (1986).

[21] S. Iijima and T. Ichihashi, Materials Transactions, JIM **31**, 582 (1990).

[22] 김근수, Analysis of Dynamic Behavior of Metal Nano-particles with Different Conductivity of Substrate using In-situ TEM : The Effect of Charge, Ph. D. thesis, 서울대학교 대학원 (2018).

[23] H. Conrad and D. Yang, Acta Mater. **55**, 6789 (2007).

[24] D. Yang and H. Conrad, Scripta Materialia **41**, 397 (1999).
[25] G. C. Bond and D. T. Thompson, Gold Bull. **33**, 41 (2000).
[26] M. Haruta, N. Yamada, T. Kobayashi, and S. Iijima, J. Catal. **115**, 301 (1989).
[27] M. Haruta, S. Tsubota, T. Kobayashi, H. Kageyama, M. J. Genet, and B. Delmon, J. Catal. **144**, 175 (1993).
[28] M. Haruta, Catal. Today **36**, 153 (1997).
[29] J. Jeon, A. Soon, J. N. Yeo, J. Park, S. Hong, K. Cho, and B. D. Yu, J. Phys. Soc. Jpn. **81**, 54601 (2012).
[30] J. Jeon and B. D. Yu, J. Korean Phys. Soc. **62**, 79 (2013).
[31] C. T. Campbell, Surf. Sci. Rep. **27**, 1 (1997).
[32] D. Y. Cha and G. Parravano, Journal of Catalysis **18**, 200 (1970).
[33] S. Galvagno and G. Parravano, J. Catal. **55**, 178 (1978).
[34] M. Valden, X. Lai, and D. W. Goodman, Science **281**, 1647 (1998).
[35] T. Urano and T. Kanaji, J. Phys. Soc. Jpn. **57**, 3403 (1988).
[36] W. H. Butler, X. G. Zhang, T. C. Schulthess, and J. M. MacLaren, Phys. Rev. B **63**, 54416 (2001).
[37] S. Yuasa, J. Phys. Soc. Jpn. **77**, 31001 (2008).
[38] S. Yuasa, T. Nagahama, A. Fukushima, Y. Suzuki, and K. Ando, Nat. Mater. **3**, 868 (2004).
[39] B. D. Yu and J. S. Kim, Phys. Rev. B **73**, 125408 (2006).
[40] J. N. Yeo, G. M. Jee, B. D. Yu, and B. C. Choi, J. Korean Phys. Soc. **52**, 1938 (2008).
[41] J. Park and B. D. Yu, Phys. Rev. B **83**, 144431 (2011).
[42] J. Park, B. D. Yu, and Y.-R. Jang, J. Korean Phys. Soc. **73**, 320 (2018).
[43] B. C. Gates, M. Flytzani-Stephanopoulos, D. A. Dixon, and A. Katz, Catal. Sci. Technol. **7**, 4259 (2017).
[44] F. Buenda, A. T. Anzaldo, C. Vital, and M. R. Beltrn, J. Chem. Phys. **152**, 24303 (2020).
[45] I. Ro, J. Resasco, and P. Christopher, ACS Catal. **8**, 7368 (2018).
[46] L. Liu and A. Corma, Chem. Rev. **118**, 4981 (2018).
[47] S. Wei, X.-P. Fu, W.-W. Wang, Z. Jin, Q.-S. Song, and C.-J. Jia, J. Phys. Chem. C **122**, 4928 (2018).
[48] T. Kropp, Z. Lu, Z. Li, Y.-H. C. Chin, and M. Mavrikakis, ACS Catal. **9**, 1595 (2019).
[49] S. Tosoni and G. Pacchioni, ChemCatChem **11**, 73 (2019).
[50] P. Novello, C. V. Varanasi, and J. Liu, ACS Catal. **9**, 578 (2019).
[51] J. G. Wang and B. Hammer, Phys. Rev. Lett. **97**, 5 (2006).
[52] H. Hkkinen and U. Landman, J. Am. Chem. Soc. **123**, 9704 (2001).
[53] L. D. Socaciu, J. Hagen, T. M. Bernhardt, L. Wste, U. Heiz, H. Hkkinen, and U. Landman, J. Am. Chem. Soc. **125**, 10437 (2003).
[54] B. Yoon, H. Hkkinen, U. Landman, A. S. Wrz, J. M. Antonietti, S. Abbet, K. Judai, and U. Heiz, Science **307**, 403 (2005).
[55] A. Sanchez, S. Abbet, U. Heiz, W. D. Schneider, H. Hkkinen, R. N. Barnett, and U. Landman, J. Phys. Chem. A **103**, 9573 (1999).
[56] G. Pacchioni, L. Giordano, and M. Baistrocchi, Physical Review Letters **94**, 226104 (2005).
[57] M. Sterrer, T. Risse, U. Martinez Pozzoni, L. Giordano, M. Heyde, H.-

P. Rust, G. Pacchioni, and H.-J. Freund, Phys. Rev. Lett. **98**, 096107 (2007).
[58] M.-J. Kim *et al.*, Applied Materials Today **21**, 100874 (2020).
[59] G. Kresse and J. Hafner, Phys. Rev. B **47**, 558 (1993).
[60] G. Kresse and J. Furthmller, Phys. Rev. B **54**, 11169 (1996).
[61] J. P. Perdew, K. Burke, and M. Ernzerhof, Phys. Rev. Lett. **77**, 3865 (1996).
[62] P. E. Blchl, Phys. Rev. B **50**, 17953 (1994).
[63] S. Kibey, J. B. Liu, D. D. Johnson, and H. Sehitoglu, Acta Mater. **55**, 6843 (2007).
[64] M. Topsakal and S. Ciraci, Physical Review B **85**, 045121 (2012).
[65] C. Zhang, R. K. Kalia, A. Nakano, P. Vashishta, and P. S. Branicio, Journal of Applied Physics **103**, 083508 (2008).
[66] P. A. Zhilyaev and A. V. Yanilkin, Russian Metallurgy (Metally) **2012**, 879 (2012).
[67] E. Tochigi, N. Shibata, A. Nakamura, T. Mizoguchi, T. Yamamoto, and Y. Ikuhara, Acta Mater. **58**, 208 (2010).
[68] E. Tochigi, A. Nakamura, N. Shibata, and Y. Ikuhara, Crystals **8** (2018).
[69] J. Castaing, A. He ‡, K. P. D. Lagerlöf, and A. H. Heuer, Philos. Mag. **84**, 1113 (2004).
[70] J. Castaing, A. Muñoz, D. Gomez Garcia, and A. Dominguez Rodriguez, Materials Science and Engineering: A **233**, 121 (1997).
[71] J. B. Bilde-Sørensen, B. F. Lawlor, T. Geipel, P. Pirouz, A. H. Heuer, and K. P. D. Lagerlo¨f, Acta Mater. **44**, 2145 (1996).
[72] P. Pirouz, B. F. Lawlor, T. Geipel, J. B. Bilde-Sørensen, A. H. Heuer, and K. P. D. Lagerlo¨f, Acta Mater. **44**, 2153 (1996).
[73] K. P. D. Lagerlöf, A. H. Heuer, J. Castaing, J. P. Rivière, and T. E. Mitchell, J. Am. Ceram. Soc. **77**, 385 (1994).
[74] W.-K. Youn, S.-S. Lee, J.-Y. Lee, C.-S. Kim, N.-M. Hwang, and S. Iijima, J. Phys. Chem. C **118**, 11946 (2014).
[75] S.-w. Park, G.-s. Jang, K.-s. Kim, and N.-m. Hwang, Electron. Mater. Lett. **16**, 72 (2020).
[76] A. V. Matveev, K. M. Neyman, I. V. Yudanov, and N. Rsch, Surf. Sci. **426**, 123 (1999).
[77] A. Bogicevic and D. R. Jennison, Surf. Sci. **437**, L741 (1999).
[78] J. Park and B. D. Yu, Journal of the Korean Physical Society **53**, 1976~1981 (2008).
[79] P. Hohenberg and W. Kohn, Phys. Rev. **136**, B864 (1964).
[80] W. Kohn and L. J. Sham, Phys. Rev. **140**, A1133 (1965).
[81] R. W. G. Wyckoff, *Crystal Structures, 2nd ed.* (Interscience, 1965).
[82] G. Henkelman, B. P. Uberuaga, and H. Jnsson, J. Chem. Phys. **113**, 9901 (2000).
[83] V. L. Deringer, A. L. Tchougreff, and R. Dronskowski, J. Phys. Chem. A **115**, 5461 (2011).
[84] R. Dronskowski and P. E. Bloechl, J. Phys. Chem. **97**, 8617 (1993).
[85] S. Maintz, V. L. Deringer, A. L. Tchougreff, and R. Dronskowski, 2016), pp. 1030.
[86] J. W. Yang, J. H. Park, M. G. Byun, J. Park, B. D. Yu, and N. M. Hwang, Diam. Relat. Mater. **107**, 107875 (2020).

[87] R. F. W. Bader, *Atoms in Molecules: A Quantum Theory* (Oxford University Press New York, 1990).
[88] G. Henkelman, A. Arnaldsson, and H. Jnsson, Comput. Mater. Sci. **36**, 354 (2006).
[89] W. Tang, E. Sanville, and G. Henkelman, J. Phys. Condens. Matter **21**, 84204 (2009).
[90] J. Jeon, A. Soon, J. Park, S. Hong, K. Cho, and B. D. Yu, J. Phys. Soc. Jpn. **82**, 34603 (2013).
[91] D. Ricci, A. Bongiorno, G. Pacchioni, and U. Landman, Physical Review Letters **97**, 036106 (2006).
[92] P. Frondelius, H. Häkkinen, and K. Honkala, New Journal of Physics **9**, 339 (2007).
[93] V. Simic-Milosevic *et al.*, Physical Review B **78**, 235429 (2008).
[94] V. Simic-Milosevic *et al.*, Journal of the American Chemical Society **130**, 7814 (2008).
[95] J. Park and B. D. Yu, J. Phys. Soc. Jpn. **79**, 74718 (2010).
[96] A. Del Vitto, G. Pacchioni, F. Delbecq, and P. Sautet, J. Phys. Chem. B **109**, 8040 (2005).
[97] C. Inntam, L. V. Moskaleva, K. M. Neyman, V. A. Nasluzov, and N. Rsch, Appl. Phys. A. **82**, 181 (2006).
[98] D. Shan, Z. Yanxing, Z. Xilin, M. Jianjun, and Y. Zongxian, Appl. Surf. Sci. **426**, 554 (2017).
[99] J. H. Park, J. W. Yang, M. G. Byun, N. M. Hwang, J. Park, and B. D. Yu, J. Phys. Soc. Japan **90**, 034602 (2021).
[100] P. Giannozzi, S. de Gironcoli, P. Pavone, and S. Baroni, Physical Review B **43**, 7231 (1991).
[101] X. Gonze and C. Lee, Physical Review B **55**, 10355 (1997).
[102] T. Atsushi and T. Isao, Scripta Materialia **108**, 1 (2015).

국문 초록

제일원리 계산을 사용하여 다양한 시스템에서 재료의 하전 연구를 진행하였다.

금속을 시뮬레이션하기 위해 모델 시스템으로서 Au(111) 슬래브 모델을 사용하였다. Au(111)가 양의 전하를 띠면 표면 과전하에 의해 쿨롱 반발이 발생한다. 때문에 슬래브 두께가 확장되며 잔류 응력이 감소한다. 이러한 확장으로 인해 적층 결함 형성 장벽이 감소하게 된다. 이는 하전이 플라스틱 변형을 촉진한다는 것을 의미한다.

세라믹을 시뮬레이션하기 위해 모델 시스템으로서 α−Al2O3가 사용되었다. 캐리어 농도를 변경하면 양 전하와 음 전하 모두 활성화 장벽, 적층 결함 에너지 및 적층 결함을 생성하는 데 필요한 전단 응력이 감소한다. 음전하는 Basal 슬립에서, 양전하는 Pyramidal 슬립에서 더 큰 효과를 낸다. 두 종류의 Prismatic 슬립에서 하전될 때의 GSF 에너지의 차이는 기초 슬립과 피라미드 슬립의 에너지와 비교했을 때 작다.

밀도 기능 이론에 기초한 Ab−initio 총 에너지 및 전자 구조 계산을 사용하여, MgO(100)위의 Au^0, Au+ 및 Au^- 를 비교하여 금 adatom의 흡착 및 확산 특성을 조사하였다. MgO(100)에서 Au^+의 가장 안정적인 흡착 부위는 Au^0의 흡착 부위와 일치하는 O 원자 위이고, 반면 Au^- 의 가장 안정적인 흡착 부위는 Mg 원자 위이다. MgO(100)에서 Au^+의 표면 확산 장벽은 0.30 eV로, Au^0(0.25 eV) 보다 크다. Au^-의 경우 표면 확산 장벽은 0.03 eV 로 낮다. 전하 재배열, Bader charge, 전자 구조, 원자 결합의 특징에 대한 상세한 분석도 수행되었다. 이러한 결과는 Au on MgO(100)의 흡착 및 확산 속성에서 Au adatom의 하전 상태의 중요한 역할을 보여준다.

ab−initio 계산을 사용하여, MgO(100) 표면의 하전된 Au dimer(Au_2^+ 및 Au_2^-)의 흡착 및 확산 특성을 조사하였고, Au_2^0의 흡착 및 확산 특성을 비교하였다. MgO(100)에서 Au_2^+의 가장 선호하는 흡착 구조는 Au_2^0과 일치하는 표면 O 원자의 직립 구조이다. MgO(100)에서 Au_2^+의

표면 확산은 Au_2^0(0.69eV)보다 장벽 높이가 0.42eV 낮은 leapfrog 방법으로 발생한다. Au_2^-의 가장 안정적인 흡착 구조는 두 개의 표면 Mg 원자 위에 평형구조이다. Au_2^-의 표면 확산은 Au_2^+와 Au_2^0의 확산 장벽보다 훨씬 낮은 0.10~0.15 eV 범위의 장벽 높이로 Hopping 및 Walking 에 의해 진행될 수 있다. 또한, Au_2^0, Au_2^+, Au_2^-의 전자 구조와 전하 분포에 대한 자세한 정보도 제시된다.

MgO(100)에서 하전 되지 않은 것과 하전 된 Au와 Au_2의 진동 스펙트럼을 ab-initio 밀도 함수 섭동 이론을 사용하여 조사하였다. 계산된 진동 스펙트럼은 MgO(100)에서 Au 및 Au_2의 하전 상태와 관련된 진동 특징을 보였다. MgO(100)의 Au와 Au_2의 평면에 수직 및 평행 모드에 대한 추가 분석을 수행하여 Au 모드를 포함하는 진동 모드를 추출했다. 이러한 모드들은 MgO(100)에서 Au와 Au_2의 충전 상태를 실험적으로 설명하는 데 중요한 정보를 제공한다.